Cell Reports
Physical Science

Article

A subcellular-specific iridium complex boosting cuproptosis for cancer theranostics

Graphical abstract

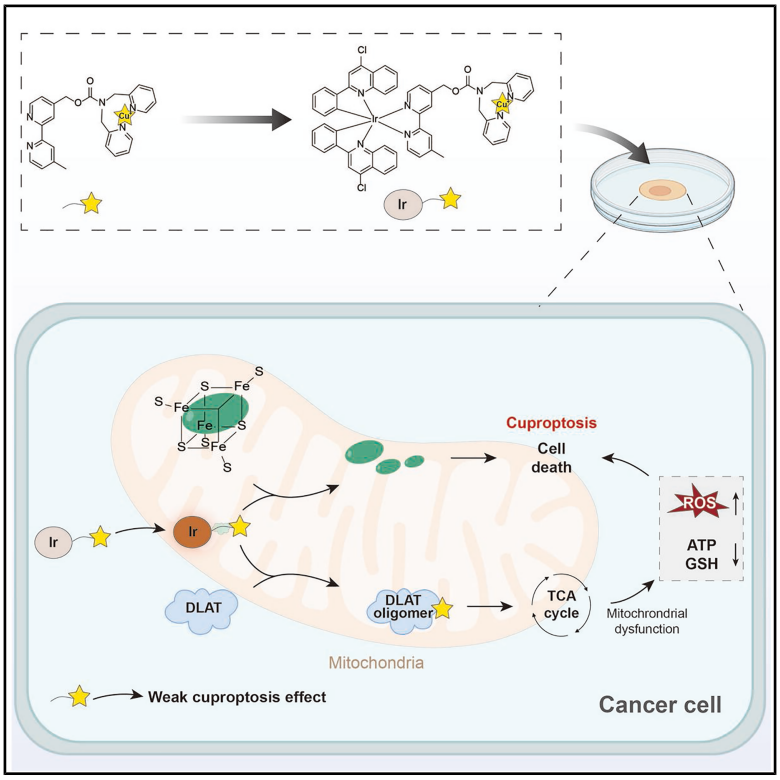

Highlights

- The iridium(III) complex enables mitochondrion-targeted Cu^{+} delivery and imaging
- The complex amplifies cuproptosis through the accumulation of Cu^{+} in mitochondria
- The complex triggers the oligomerization of DLAT along with ROS production
- High *in vivo* biocompatibility is demonstrated in Kunming mice

Authors

Jianxiong Du, Ling Wang, Lei Wu, Jin-Biao Liu, Chung-Hang Leung, Wanhe Wang

Correspondence

liujinbiao@jxust.edu.cn (J.-B.L.), duncanleung@um.edu.mo (C.-H.L.), whwang0206@nwpu.edu.cn (W.W.)

In brief

Inducing cuproptosis is a promising anticancer strategy through copper-dependent programmed cell death, yet current copper delivery systems lack efficacy and have poor trackability. Du et al. report an iridium(III) complex for tracking and delivering Cu^{+} ions into mitochondria of triple-negative breast cancer to boost cuproptosis.

Du et al., 2025, Cell Reports Physical Science 6, 102592
May 21, 2025
https://doi.org/10.1016/j.xcrp.2025.102592

CellPress

Cell Reports
Physical Science

CellPress
OPEN ACCESS

Article

A subcellular-specific iridium complex boosting cuproptosis for cancer theranostics

Jianxiong Du,[1,3,5] Ling Wang,[2,5] Lei Wu,[2] Jin-Biao Liu,[3,*] Chung-Hang Leung,[2,6,*] and Wanhe Wang[1,4,*]
[1]Institute of Medical Research, Northwestern Polytechnical University, 127 West Youyi Road, Xi'an, Shaanxi 710072, China
[2]State Key Laboratory of Quality Research in Chinese Medicine, Institute of Chinese Medical Sciences, University of Macau, Macao 999078, China
[3]School of Metallurgy and Chemical Engineering, Jiangxi University of Science and Technology, 86 Hongqi Road, Ganzhou, China
[4]Research & Development Institute of Northwestern Polytechnical University in Shenzhen, 45 South Gaoxin Road, Shenzhen 518057, China
[5]These authors contributed equally
[6]Lead contact
*Correspondence: liujinbiao@jxust.edu.cn (J.-B.L.), duncanleung@um.edu.mo (C.-H.L.), whwang0206@nwpu.edu.cn (W.W.)
https://doi.org/10.1016/j.xcrp.2025.102592

SUMMARY

Cuproptosis, a copper (Cu)-dependent anticancer mechanism, faces challenges in Cu delivery and tracking. Here, we report the first iridium(III) complex with Cu^+ ion-chelating properties designed for the tracking and delivery of Cu^+ ions into the mitochondria of triple-negative breast cancer (TNBC) cells to induce cuproptosis. The probe exhibits a specific luminescence binding affinity to Cu^+ ions (K_d of 7.64×10^{-2} μM, 1:1 stoichiometry). The Cu^+-loaded probe induces oligomerization of the cuproptosis marker DLAT, disrupting the tricarboxylic acid (TCA) cycle, elevating reactive oxygen species (ROS), depleting adenosine triphosphate (ATP) and glutathione (GSH), and impairing the iron-sulfur (Fe-S) cluster protein lipoyl synthase (LIAS), collectively amplifying cuproptosis to kill TNBC cells. *In vivo* studies confirmed negligible toxicity of the Cu^+-loaded probe in mice, highlighting its potential application in preclinical studies. This work provides a strategy for the development of efficient theranostic probes that act by boosting cuproptosis.

INTRODUCTION

Transition metals play an essential role in all living systems, serving as structural stabilizers of all DNA, RNA, and more than a third of all proteins.[1] Their presence is essential for the functioning of certain enzymes, oxygen transport, and energy transfer and signaling.[2,3] However, excessive amounts of transition metals can cause irreversible damage to living systems. Tsvetkov et al. revealed that copper (Cu) toxicity disrupts specific mitochondrial metabolic enzymes, triggering an unusual mechanism of cell death that can be facilitated by Cu ionophores, such as the experimental drug eresclomol, which delivers extracellular Cu to mitochondria.[4,5] Cu enrichment also leads to changes in upstream factors such as lipoyl synthase (LIAS) and ferric redox protein 1 (FDX1), causing lipoylation of enzymes such as dihydrolipoamide *S*-acetyltransferase (DLAT). Cu also triggers protein oligomerization by binding to lipoylated DLAT.[1] Cu can also induce aggregation of mitochondrial lipoylated proteins and destabilize iron-sulfur cluster proteins in the tricarboxylic acid (TCA) cycle.[6] Thus, disruption of Cu homeostasis in cells can result in programmed cell death,[4] providing a novel therapeutic strategy to combat cancer.[7–9]

Although Cu ion concentrations are higher in various cancer cells than in normal cells, they are still too low to achieve therapeutic effects.[10,11] Moreover, non-specific excess Cu is toxic to normal cells, highlighting the need for targeted delivery systems to cancer cells.[10,12] This delivery can be achieved with the aid of ionophores such as transferrin, but these can suffer from limitations, including side effects, poor biostability, and non-selectivity, making them unsuitable for clinical applications.[11] To improve Cu delivery to tumor sites, Guo et al. constructed immunotherapeutic nanoreactors that encapsulate Cu ions using polyethylene glycol modifications, releasing Cu ions in the presence of glutathione (GSH) once inside cells.[13] Cu-based nanomaterials are ideal sources for delivering Cu for evoking cuproptosis-induced cell death without the need for additional Cu loading.[14] Wang's group designed a series of functional Cu nanomaterials for eliminating drug-resistant bacteria and enhancing chemotherapeutic effects.[7–9] Small-molecule metal chelating agents have also gained attention for Cu delivery. For example, Huang et al. designed the strong chelator diethyldithiocarbamate, which forms complexes with Cu in the presence of hydrogen peroxide, achieving high cytotoxicity with low systemic toxicity.[15] Nevertheless, cuproptosis induced by both nanomaterials and small-molecule ionophores is limited by non-specific activation due to poor subcellular targetability and lack of real-time tracking.[16]

Luminescent iridium(III) complexes are emerging as promising subcellular-targeting luminophores due to their desirable imaging properties, including high photostability, bright phosphorescence, and mitochondrial targetability that arises from their intrinsic lipophilic cationicity.[17] These features make iridium(III)

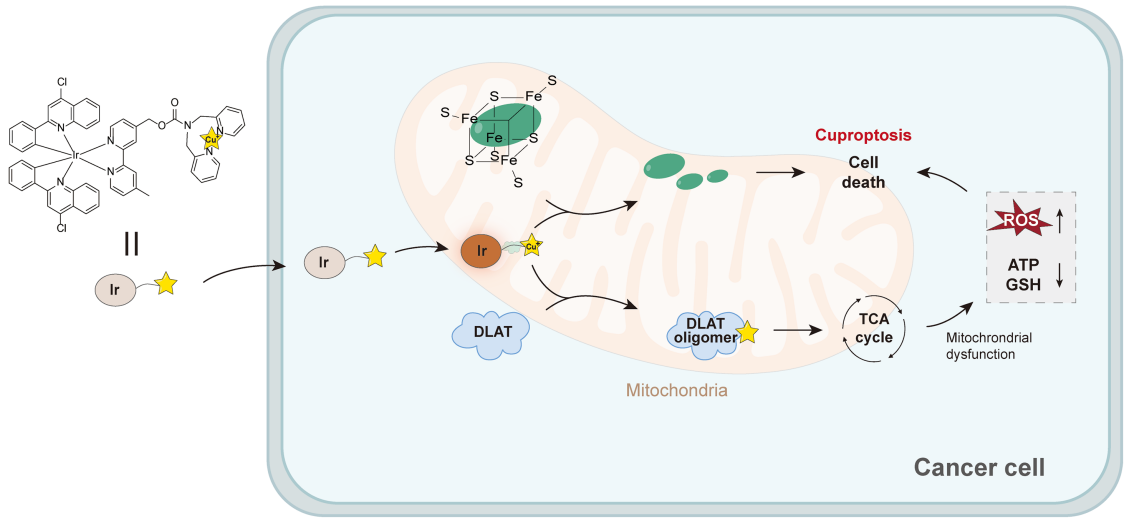

Scheme 1. Schematic of iridium(III) complex 1 for inducing cuproptosis as an anticancer theranostic probe

complexes suitable for use as mitochondrion-specific bioimaging probes and targeted bioactive compounds. In this work, we present a mitochondrion-specific iridium(III) complex-based ionophore for effectively inducing cuproptosis as an anticancer theranostic probe (Scheme 1). The complex contains a (4′-methyl-[2,2′-bipyridin]-4-yl)methyl bis(pyridin-2-ylmethyl) carbamate N^N ligand that selectively carries Cu^+ ions, thus eliminating the need to transform Cu^{2+} ions into Cu^+ ions within the cellular environment. This complex exhibits mitochondrion-specific "turn-on" luminescence in MDA-MB-231 cells. It induces strong cuproptosis through DLAT oligomerization with an antiproliferative half maximal inhibitory concentration (IC_{50}) of 0.26 μM in a serum-containing environment, along with triggering reactive oxygen species (ROS) overproduction and ATP and GSH depletion. This work establishes a versatile platform for developing cuproptosis-based theranostic agents.

RESULTS AND DISCUSSION

Design and synthesis of a luminescent cuproptosis inducer

We designed an iridium(III) complex with a dimethylpyridinamine-containing NN ligand as a Cu chelating unit for the specific binding of Cu^+ ions. In this design, the dimethylpyridinamine moiety, commonly found in existing Cu ionophores,[18,19] is connected to a widely used NN ligand, (3′-methyl-[1,1′-biphenyl]-3-yl)methanol.[15,20] The direct use of Cu^+ ionophores eliminates the need for the reduction of Cu^{2+} to Cu^+ ions, which is expected to amplify the effect of cuproptosis. The cyclometalated iridium (III) complex serves as both a mitochondrial targeting unit and a luminophore. The cyclometalating CN ligand, 4-chloro-2-phenylquinoline, is used to modulate the emission properties of the iridium(III) complex, making it suitable for imaging applications. The combination of these components is designed to efficiently deliver Cu^+ ions into the mitochondria of cancer cells, thereby inducing cuproptosis and facilitating live-cell imaging.

The synthesis of complex **1** was carried out using a convergent strategy (Figure 1A): (3′-methyl-[1,1′-biphenyl]-3-yl)methanol was activated by 4-nitrophenyl carbonochloridate to form the intermediate **S1**, which was reacted with bis(pyridin-2-yl methyl) amine to form the final NN ligand **S2**. At the same time, the C^N ligand 4-chloro-2-phenylquinoline (Clpq) was reacted with iridium(III) chloride hydrate ($IrCl_3{\cdot}xH_2O$) to give the chloro-bridged iridium(III) dimer. Finally, ligand **S2** was coordinated to the dimer to generate the final complex **1**. All intermediates and the complex were fully characterized by ^{1}H-NMR, ^{13}C-NMR, and electrospray ionization mass spectrometry (ESI-MS) (Figures S1–S9), while the purity of complex **1** was found by high-performance liquid chromatography to be over 95% (Figure S10).

Specific luminescence response and high affinity of complex 1 for Cu^+ ions

We first investigated the photophysical properties of complex **1** (10 μM) in phosphate-buffered saline (PBS) buffer (Table S1). The complex exhibited a strong absorption band at 300–400 nm, which was attributed to the π-π* transition of the ligand and the singlet metal-to-ligand charge transfer interaction, while a weaker absorption band beyond 400 nm with an absorption peak at around 460 nm presumably belonged to the triplet MLCT (^{3}MLCT) state (Figure 1B).[21–23] Complex **1** exhibits a maximum excitation at around 345 nm and a broad emission band centered near 634 nm (Figures 1C and S11), indicating a broad Stokes shift of 174 nm between its ^{3}MLCT absorption and emission maxima. This shift is much larger than that of commonly used organic dyes, which avoids interference from the excitation light source. Furthermore, the luminescence intensity of complex **1** remained stable after 35 min of continuous UV irradiation at 365 nm (Figure S12). The luminescence lifetime of complex **1** at 634 nm in acetonitrile was determined to be 878 ns (Table S1), which is much longer than that for organic dyes. Taken together, complex **1** retains the desirable photophysical properties of iridium(III) complexes.

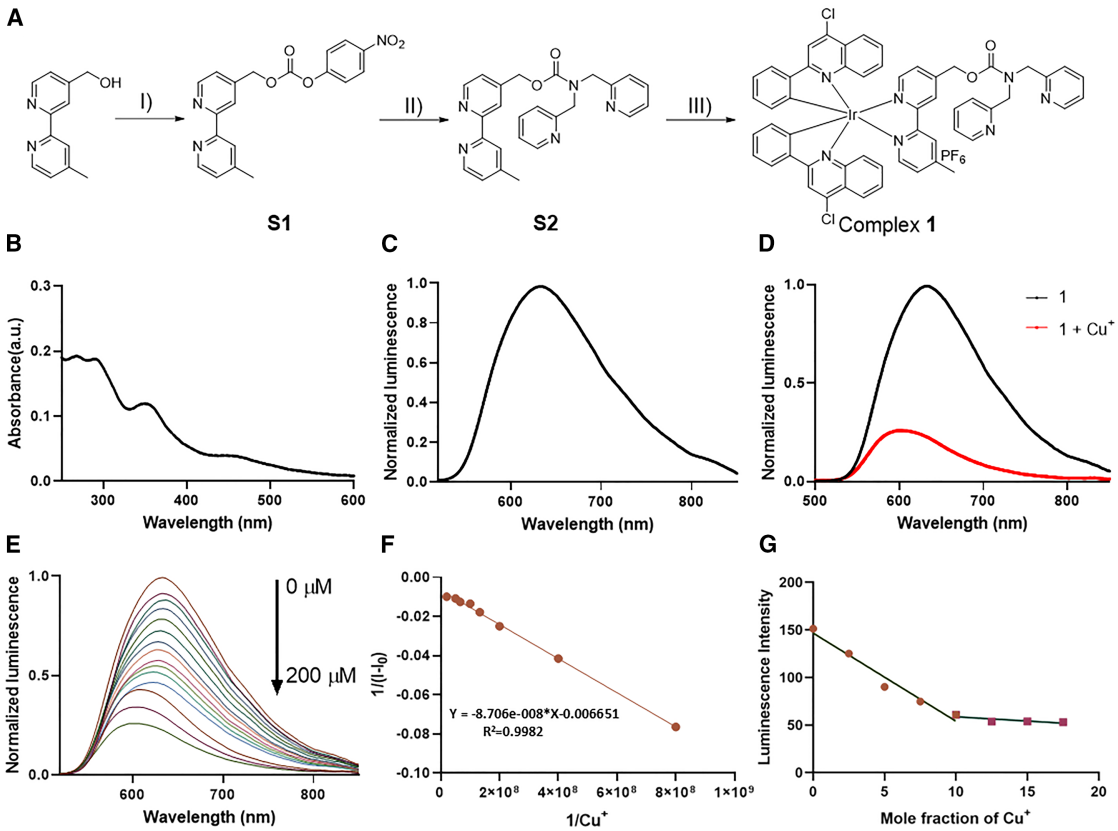

Figure 1. Synthesis and luminescence profiles of complex 1

(A) Synthesis of complex **1**. Reagents and conditions: (I) 4-nitrophenyl chloroformate, pyridine, N_2, DCM; (II) bis(pyridin-2-ylmethyl)amine, *N*,*N*-diisopropylethylamine (DIPEA), dichloromethane (DCM), overnight, 60°C; (III) $Ir_2[Clpq]_4Cl_2$, DCM/MeOH, room temperature, overnight and then addition of NH_4PF_6 for 0.5 h.

(B and C) The (B) absorption spectra and (C) emission spectra of complex **1** (10 μM) in PBS; λ_{ex} = 345 nm.

(D) Luminescence spectra of complex **1** (10 μM) with the addition of Cu^+ ions (200 μM).

(E) Luminescence spectra of complex **1** (10 μM) with various concentrations of Cu^+ ions (0–200 μM).

(F) Benesi-Hildebrand plot of complex **1** with Cu^+ ions; λ_{ex} = 345 nm and λ_{em} = 634 nm.

(G) Job plot analysis of complex **1** and Cu^+ ions in PBS. The total molar concentration of complex and Cu^+ ions is 20 μM.

We further investigated the luminescence response of complex **1** to Cu^+, taking the opportunity to track Cu^+ ions in live cancer cells. The luminescence of complex **1** was substantially quenched by the addition of Cu^+ ions, with a quenching efficiency of 75% at 200 μM (Figure 1D). We hypothesize that Cu^+ binding induces photoinduced energy transfer (PeT) in complex **1**, thus quenching its ^{3}MLCT emission.[20] The luminescence response of complex **1** to Cu^+ was further investigated using varying concentrations of Cu^+ ions (0–200 μM). Complex **1** showed a gradual decrease in luminescence with increasing Cu^+ ion concentration, which was accompanied by a slight blueshift (Figure 1E). Linear relationships were observed in the range of 0.1–1 μM and 1–10 μM with a limit of detection of 0.05 μM (Figure S13). To determine the specific luminescence response of complex **1** to Cu^+ ions, its response to metal ions and other potential cellular interference was investigated. Complex **1** showed significantly greater quenching of luminescence in the presence of Cu^+ ions compared to other metal ions, amino acids, GSH, and common protein BSA (Figure S14). Moreover, complex **1** showed a much obvious luminescence response to Cu^+ ions compared to Cu^{2+} ions. The Benesi-Hildebrand plot of $[1/(I-I_0)]$ against the reciprocal concentration of Cu^+ ion was linear, allowing the determination of the binding constant of complex **1** to Cu^+ ions as 7.64×10^{-2} μM (Figure 1F). A further Job plot analysis suggested that complex **1** forms a stable complex with Cu^+ ions at a molar ratio of 1:1 (Figure 1G). These results demonstrate that complex **1** is not only able to strongly chelate Cu^+ ions but also enables their monitoring in live-cell luminescence imaging.

Imaging of mitochondrial Cu^+ ions in TNBC cells

Encouraged by the results in solution, we examined the imaging feasibility of complex **1** in response to Cu^+ ions in the human breast epithelial cell line MCF-10A and the human triple-negative breast cancer (TNBC) cell line MDA-MB-231. Complex **1** exhibited negligible luminescence in MCF-10A cells but displayed weak luminescence in MDA-MB-231 cells (Figures 2A and 2B). Surprisingly, the addition of Cu^+ ions (10 μM) strongly enhanced the luminescence of the complex in MDA-MB-231

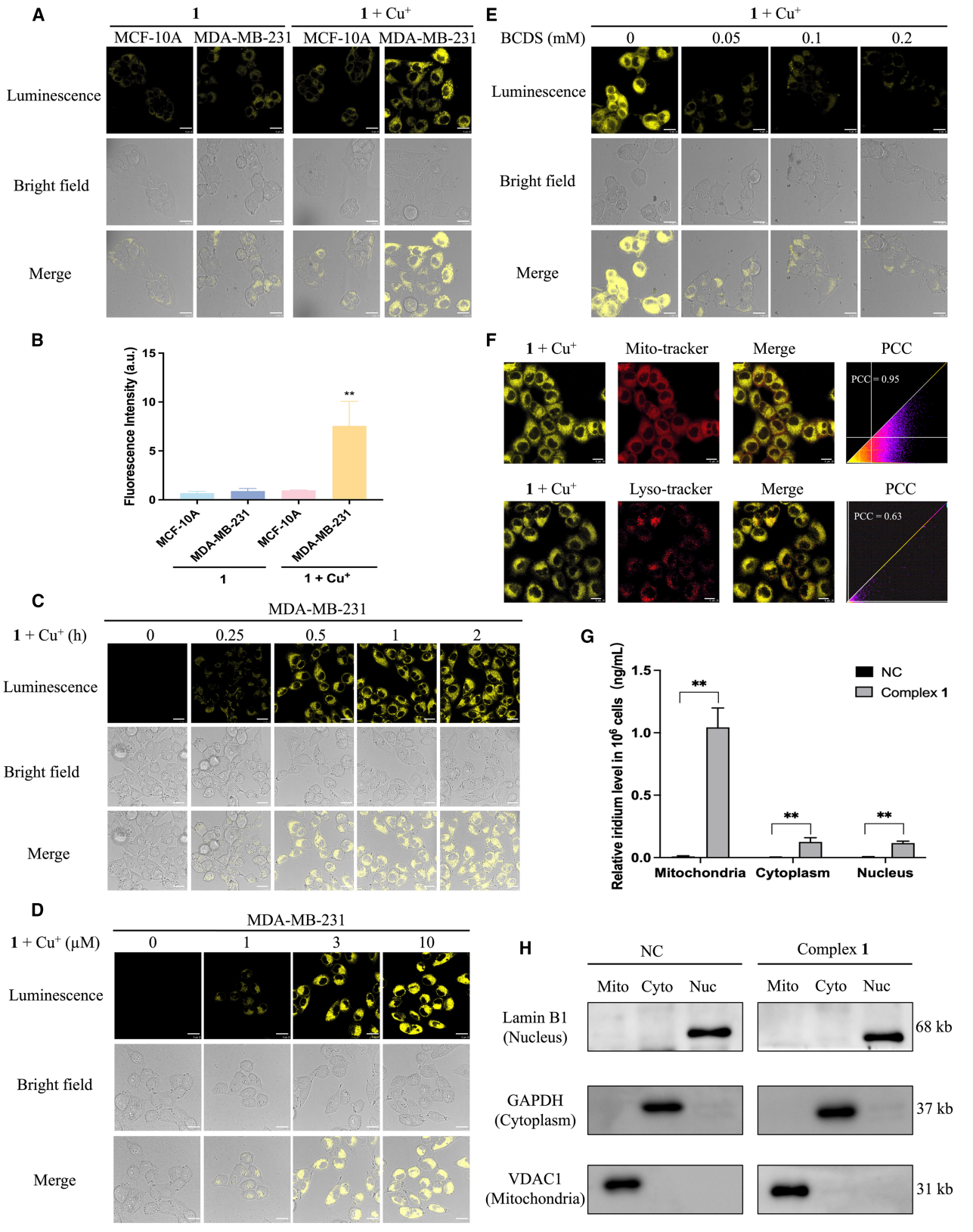

(legend on next page)

cells while only slightly increasing the luminescence in MCF-10A cells (Figures 2A and 2B). This is in contrast to the behavior in solution, where Cu^+ ions quenched the luminescence of complex **1**. We hypothesize that the Cu^+-loaded probe interacts with cellular proteins to inhibit PeT, thus restoring luminescence.[20] Indeed, the addition of FBS into complex **1** or the Cu^+-loaded probe restores or even amplifies the luminescent properties of the system, with a greater effect on the Cu^+-loaded probe compared to complex **1** alone (Figure S15). This suggests that complex **1** is responsive to Cu^+ ions present in the cellular environment, similar to the previously reported sensitivity of some Cu ionophores to Cu ions in cell culture environments.[4] Notably, complex **1** can discriminate TNBC cells from normal breast cells in the presence of Cu^+ ions, presumably due to the higher demand for Cu^+ ions in cancer cells than in normal cells.[24] Consequently, this phenomenon could contribute to the heightened luminescence observed in the Cu^+-loaded probe within the cellular environment. Moreover, the luminescence of complex **1** with Cu^+ ions clearly increased with the incubation time in TNBC cells, resulting in good imaging performance at 30 min (Figure 2C). Furthermore, the luminescence intensity of MDA-MB-231 cells was positively correlated with Cu^+ ion concentration (0–10 μM) (Figure 2D). These results confirm that complex **1** can image Cu^+ ions in cells while maintaining a very low background signal.

Bathocuproinedisulfonic acid disodium salt (BCDS) is a known chelator for Cu^+ ions. To further verify the imaging ability of complex **1** for Cu^+ ions, we used BCDS as a Cu^+ ion scavenger. With an increasing concentration of BCDS (0–200 μM), the imaging luminescence significantly decreased (Figure 2E). This aligns with the expectation that BCDS would chelate Cu^+ ions and further confirms the imaging ability of complex **1** for Cu^+ ions in MDA-MB-231 cells. Given that iridium(III) complexes generally prefer to be located in mitochondria and that Cu^+-induced cuproptosis mainly occurs in this organelle, we sought to determine the subcellular distribution of complex **1**. Using a commercial mitochondrial dye, MitoTracker Red, we observed that the yellow luminescence of complex **1** overlapped well with the red luminescence of MitoTracker Red with a Pearson correlation coefficient of 0.95 (Figure 2F). This indicates that complex **1** effectively targets mitochondria for the delivery of Cu^+ ions. We further employed inductively coupled plasma (ICP)-MS to determine the distribution of complex **1** within the cell. The results showed significant levels of complex **1** in mitochondria, with concentrations exceeding 1 ng/mL, while negligible levels were detected in the cytoplasm and nucleus (Figure 2G). The successful separation of mitochondria, cytoplasm, and nucleus was confirmed by western blotting with the markers voltage-dependent anion channel 1 (VDAC1), glyceraldehyde-3-phosphate dehydrogenase (GAPDH), and Lamin B1, respectively (Figure 2H). Together, these results indicate that complex **1** has the ability to bind and image Cu^+ ions in mitochondria.

Amplified anticancer effect of complex 1 within Cu^+ ions in TNBC cells

We evaluated the toxicity of complex **1** in MDA-MB-231 cells using the 3-(4,5-dimethylthiazol-2-yl)-2,5-diphenyltetrazolium bromide assay. As serum contains a certain level of Cu ions,[25,26] the toxicity of complex **1** was evaluated in MDA-MB-231 cells under serum-free culture conditions. Complex **1** displayed considerable cytotoxicity with an IC_{50} of 6.03 μM after 24 h (Figure 3A). Furthermore, the addition of Cu^+ ions enhanced the cytotoxicity of complex **1**, lowering its IC_{50} to 1.91 μM, indicating a key role of Cu^+ ions in the cytotoxicity of this complex (Figure 3B). After adding 1% serum under the same conditions, the cytotoxicity of complex **1** and the Cu^+-loaded probe **1** were enhanced by about 9-fold and 7-fold, respectively, decreasing the IC_{50} values to 0.68 μM and 0.26 μM (Figures S16A and S16B). These data suggested that the presence of serum could provide additional Cu^+ ions or facilitate the delivery of Cu^+ ions by complex **1**.

To further investigate the effect of Cu^+ ions on the cytotoxicity of complex **1**, we tested the cytotoxicity of the chelating N^N ligand **S2**. The results showed that the ligand alone had no obvious cytotoxicity in the absence of Cu^+ ions (Figure 3C), but its cytotoxicity considerably increased to 19.95 μM with the addition of Cu^+ ions (Figure 3D), which is consistent with the trend for complex **1**. As a control, Cu^+ ions alone showed an IC_{50} of over 100 μM, indicating the importance of ionophores in facilitating the cytotoxicity of Cu^+ (Figure 3E). Of note, the cytotoxicity of ligand **S2** with Cu^+ ions is much lower than that of complex **1**, which could be mainly attributed to mitochondrial targetability of iridium(III) complexes. This was verified by an ICP-MS

Figure 2. Luminescence imaging of complex 1 and the Cu^+-loaded probe 1 and the subcellular distribution of complex 1 in MDA-MB-231 cells

(A) Confocal microscopy images of MCF-10A and MDA-MB-231 cells incubated with complex **1** or the Cu^+-loaded probe **1**. The cells were pretreated with complex **1** or the Cu^+-loaded probe **1** (10 μM) for 1 h. Scale bar: 10 μm.

(B) The corresponding mean luminescence intensity measured in each cell line. The images were obtained using ImageJ software. The data are presented as mean ± SD. $n = 3$, $^{**}p < 0.01$.

(C) MDA-MB-231 cells were incubated in the Cu^+-loaded probe **1** (10 μM) for 0–2 h. $\lambda_{ex}/\lambda_{em}$ = 405/549–649 nm. Scale bar: 10 μm.

(D) Luminescence images of MDA-MB-231 cells incubated with 0–10 μM of the Cu^+-loaded probe **1** for 1 h. $\lambda_{ex}/\lambda_{em}$ = 405/549–649 nm. Scale bar: 10 μm.

(E) Luminescence images of MDA-MB-231 cells pretreated with BCDS (0, 0.05, 0.1, and 0.2 mM) and then incubated with 10 μM the Cu^+-loaded probe **1**. $\lambda_{ex}/\lambda_{em}$ = 405/549–649 nm. Scale bar: 10 μm.

(F) Luminescence images of the cellular distribution of complex **1** (10 μM) in MDA-MB-231 cells. Yellow, the Cu^+-loaded probe **1** (10 μM); red, MitoTracker Red (100 nM) or LysoTracker Red (50 nM). Cell images were detected at $\lambda_{ex}/\lambda_{em}$ = 405/549–649 nm for complex **1** and at $\lambda_{ex}/\lambda_{em}$ = 525/570–700 nm for MitoTracker Red or LysoTracker Red.

(G) ICP-MS comparison of iridium levels in the mitochondria, nucleus, and cytoplasm of MDA-MB-231 cells after treatment with complex **1** (10 μM) for 2 h. Data are presented as mean ± SD. $n = 3$, $^{**}p < 0.01$.

(H) Total protein expression of VDAC1, Lamin B1, and GAPDH was analyzed in isolated organelle lysates using western blotting. This experiment was repeated three times with similar results.

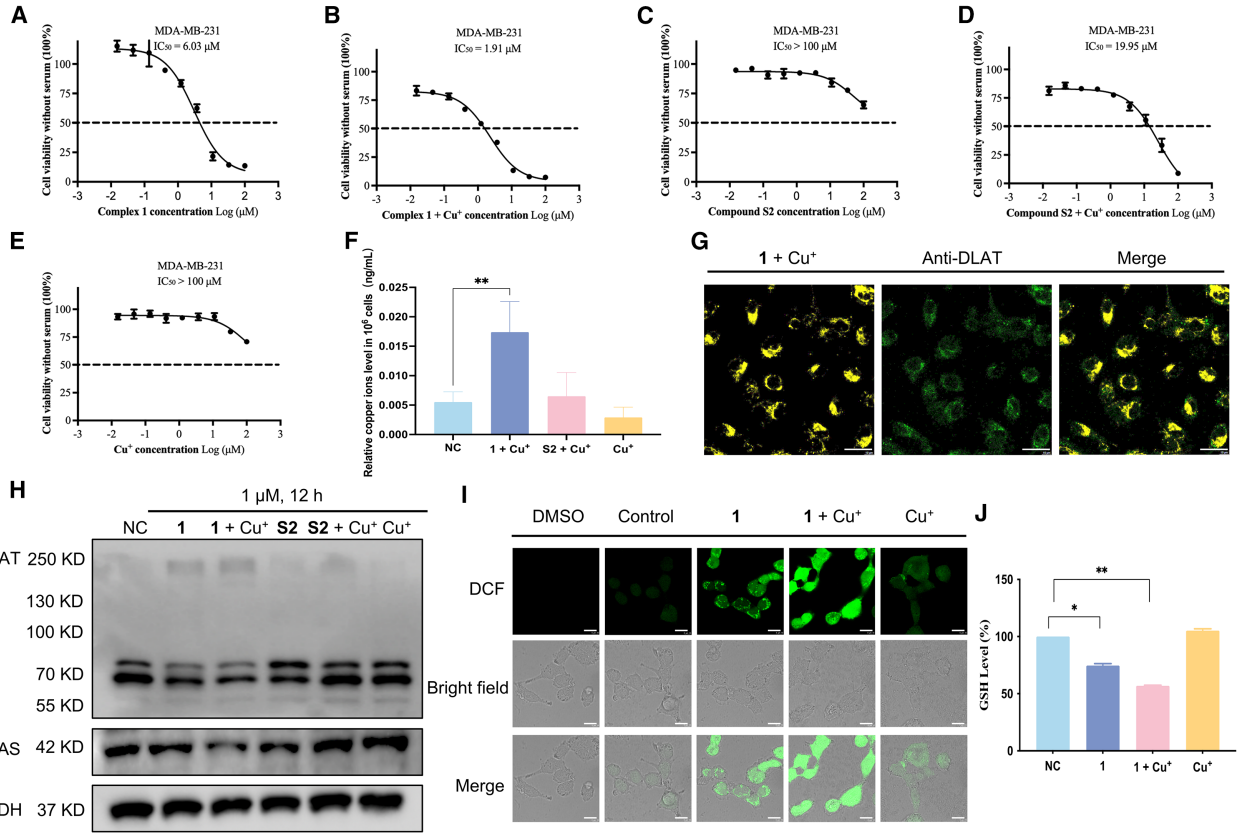

Figure 3. The cytotoxicity effect of the Cu^+-loaded probe 1 on MDA-MB-231 cells and its mechanism study

(A–E) Serum-free cultured MDA-MB-231 cells were incubated with (A) complex **1**, (B) the Cu^+-loaded probe **1**, (C) compound **S2**, (D) the Cu^+-loaded compound **S2**, and (E) Cu^+ for 24 h, and cell viability was measured. Complex **1** and compound **S2** were premixed with Cu^+ in a concentration ratio of 1:1, respectively.

(F) Uptake of Cu by the Cu^+-loaded probe **1**, **S2** + Cu^+, and Cu^+ in the mitochondria of MDA-MB-231 cells and ICP-MS comparison of Cu levels in the mitochondria of MDA-MB-231 cells after treatment with the Cu^+-loaded probe **1**, the Cu^+-loaded compound **S2**, and Cu^+ (10 μM) for 2 h. Data are presented as mean ± SD. $n = 3$. $^{**}p < 0.01$.

(G) The Cu^+-loaded probe **1** could bind to DLAT in MDA-MB-231 cells. Shown are confocal microscopy images of MDA-MB-231 cells incubated with the Cu^+-loaded probe **1** (10 μM, 1 h) and anti-DLAT. Scale bar: 10 μm.

(H) DLAT expression in MDA-MB-231 cells with treatment of 1 μM complex **1**, the Cu^+-loaded probe **1**, compound **S2**, compound **S2** + Cu^+, and Cu^+ for 12 h.

(I) Complex **1** and the Cu^+-loaded probe **1** had a significant effect on ROS elevation. Scale bar: 10 μm.

(J) The level of GSH in MDA-MB-231 cells treated with complex **1** and the Cu^+-loaded probe **1** for 12 h. $^{*}p < 0.05$, $^{**}p < 0.01$.

experiment, which showed that the mitochondrial level of Cu was much higher for the Cu^+-loaded probe **1** than the Cu^+-loaded compound **S2** or Cu^+, indicating that **1** facilitates the transport of Cu^+ into mitochondria (Figure 3F). These results support the hypothesis that complex **1** amplifies the cytotoxic effects of Cu^+ ions through mitochondrial delivery.

We also used the Cu^+ ion chelator BCDS to verify the cuproptosis effect of complex **1**.[27] We first confirmed that 200 μM BCDS alone had little effect on cell viability (Figure S17A). Then, the Cu^+-loaded probe **1** at its IC_{50} concentration was added to serum-free MDA-MB-231 cells alongside different concentrations of BCDS (0–200 μM). The results showed that the chelation of Cu^+ ions by BCDS rescued cells from cytotoxicity induced by the Cu^+-loaded probe **1** by up to 75.81% at 200 μM BCDS (Figure S17B). This is consistent with previous reports that Cu^+ chelation can rescue cells from Cu^+-induced cell death.[4,28] A similar trend was also observed for compound **S2** + Cu^+ (Figure S17C), further confirming the targeted delivery capability of complex **1**. Together, our results show that complex **1** induces Cu^+-associated cell death.

Inducing TNBC cell death by complex 1 through cuproptosis

The vast majority of current Cu delivery strategies rely on Cu^{2+} ions as sources, which are transported to cancer cells and then reduced to more toxic Cu^+ by intracellular mitochondrial FDX1, leading to oligomerization of the lipoylated protein DLAT, thereby inducing cell death.[11,13,27,29,30] In the present study, Cu^+ ions were directly delivered to cells with the assistance of complex **1**, providing excellent anticancer effects even when cancer cells have low expression of FDX1. DLAT, as a key component of the pyruvate dehydrogenase complex, is crucial for maintaining the normal function of the TCA cycle. In an environment of excess Cu^+ ions, Cu^+ ions specifically

bind to lipoic acid-modified proteins in the TCA cycle, triggering the oligomerization of these proteins. This oligomerization process disrupts the normal metabolic activities of the TCA cycle, induces a protein toxicity stress response within the cell, and ultimately leads to cell death, which is a hallmark of cuproptosis.[4,6,31–33]

To investigate the anticancer mechanism of the complex as a cuproptosis inducer, we performed a DLAT immunofluorescence experiment comparing the luminescence of the Cu^+-loaded probe **1** with the fluorescence of a DLAT antibody detection kit (anti-DLAT). The results showed a high overlap between the luminescence of the Cu^+-loaded probe **1** and the immunofluorescence of DLAT in MDA-MB-231 cells (Figure 3G). This indicates that complex **1** can deliver Cu^+ to bind to the marker protein for Cu-induced cell death, demonstrating its potential to induce cuproptosis. Moreover, a western blot experiment demonstrated DLAT aggregation with the presence of the Cu^+-loaded probe **1** at 1 μM, whereas negligible aggregation of DLAT was observed for compound **S2**, compound **S2** + Cu^+, and Cu^+ at the same concentrations (Figure 3H). Interestingly, complex **1** alone also triggers the aggregation of DLAT, consistent with its ability to chelate Cu^+ from serum. Additionally, the Cu^+-loaded probe **1** could significantly reduce the expression of LIAS (Figure 3H), a iron-sulfur (Fe-S) cluster protein that is downregulated by Cu^+ interference. This results in the loss of the Fe-S cluster proteins, thereby enhancing mitochondrial protein toxicity and triggering eventual cell death.[1,6] This process also disrupts the TCA cycle, which, in turn, interferes with mitochondrial function. To further validate the key role of mitochondria in cuproptosis, we investigated the effect of the Cu^+-loaded probe **1** on mitochondrial ATP production. The TCA cycle in mitochondria is a core process of cellular energy metabolism, and its normal operation is crucial for ATP production. The results showed that the Cu^+-loaded probe **1** significantly inhibits mitochondrial ATP production (Figure S18), indicating that cuproptosis disrupts mitochondrial energy metabolism by interfering with the TCA cycle. Overall, these findings indicate that complex **1** could deliver Cu^+ and promote DLAT oligomerization and loss of Fe-S cluster proteins, resulting in proteotoxic stress and impaired mitochondrial function, ultimately leading to cell death.

Additionally, mitochondria are the regulatory centers for cellular redox balance, and mitochondrial dysfunction caused by cuproptosis leads to abnormal ROS metabolism within the cell.[18,28] Cuproptosis is generally associated with high levels of ROS, so we further investigated ROS generation in MDA-MB-231 cells incubated with the Cu^+-loaded probe **1** using the general ROS indicator 2',7'-dichlorofluorescein (DCF). The addition of Cu^+ to complex **1** induced significant ROS generation, as shown by an increase in DCF fluorescence (Figure 3I). Complex **1** alone also induced considerable ROS production, indicating its chemotherapeutic activity and ability to amplify cuproptosis. In contrast, the addition of Cu^+ ions alone induced weak fluorescence in MDA-MB-231 cells, presumably due to their poor cellular penetration.

The level of GSH in cancer cells is generally higher than in normal cells, and GSH is also an excellent Cu chelator. GSH depletion can reflect the delivery efficiency of Cu ions, and low levels of GSH also induce cell death. Therefore, we evaluated GSH levels after the addition of complex **1** and/or Cu^+ in MDA-MB-231 cells. The results showed that the GSH content was reduced to about 50% by the Cu^+-loaded probe **1**, whereas Cu^+ ions alone induced a slight increase in GSH, indicating that Cu^+ ions alone have difficulty to freely enter cells (Figure 3J). Intriguingly, the presence of complex **1** alone also decreased GSH levels, indicating that complex **1** has a synergistic anticancer effect with cellular Cu^+ ions. Taken together, these results indicate that, during complex **1**-induced cuproptosis, intracellular ROS levels are significantly increased, while the levels of GSH decrease, further damaging mitochondria and leading to oxidative stress-induced death of tumor cells.

In vivo biocompatibility study

In vivo biosafety is a key parameter for the use of complex **1** in living organisms, increasing its potential as a preclinical candidate. Therefore, we examined the *in vivo* biosafety profile of the Cu^+-loaded probe **1**. Kunming mice were intraperitoneally injected with three different doses of the Cu^+-loaded probe **1** (2.5, 5, and 10 mg kg^{-1}), and their weight changes were recorded over a duration of 14 days. The groups treated with the Cu^+-loaded probe **1**, even at the highest dose of 10 mg kg^{-1}, had a similar weight change profile as the control group (Figure S19A). Meanwhile, the major organs of the mice—heart, liver, spleen, lungs, and kidneys—were harvested for histopathological analysis after treatment. The results showed that there were no major alterations or signs of toxicity of the major organs in the treatment groups compared to the control group (Figure S19B). Taken together, these findings confirm the biocompatibility of complex **1** for *in vivo* studies in the future.

Current drugs for cuproptosis are limited by their low efficacy, mainly due to the poor delivery of extracellular Cu ions into mitochondria. Moreover, currently available Cu delivery strategies lack visualization capabilities. Most reported methods depend on the delivery of Cu^{2+} ions; thus, their cuproptosis effects are also limited by the cellular reduction of Cu^{2+} ions. To enable efficient cuproptosis, we designed a luminescent iridium(III) complex-based ionophore for the direct delivery and visualization of Cu^+ ions into mitochondria. Unlike previously reported Cu ionophores,[34] this iridium(III)-based ionophore specifically localizes in the mitochondria of TNBC cells, facilitating the accumulation of a high concentration of mitochondrial Cu^+ ions. Complex **1** also retains the optical characteristics of iridium(III) complexes, with a wide Stokes shift, long luminescence lifetime, and robust photostability, which compares favorably to traditional organic dyes. The dimethylpyridinamine moiety of the probe enables it to bind to Cu^+ ions at a ratio of 1:1 with a submicromolar K_d. Additionally, complex **1** exhibits a selective luminescence response to Cu^+ ions, a feature that is not accessible to previous cuproptosis molecules. Notably, the complex has an opposite luminescence response to Cu^+ ions in aqueous buffer (turn off) and serum (turn on). This activation mode provides a better signal-to-background ratio for imaging compared to turn-on probes, as the complex showed negligible luminescence in TNBC or MCF-10A cells in the absence of Cu^+ ions. Moreover, interaction with serum proteins also helps to deliver Cu^+ ions

into TNBC cells, allowing the probe to selectively light up TNBC cells in the presence of Cu^+ ions. The monitoring function of this probe was further demonstrated by the addition of BCDS (a Cu chelator), which quenched the luminescence of the probe with Cu^+ ions, confirming its monitoring capability.

This probe has high mitochondrial targetability due to its cationic lipophilicity. The addition of Cu^+ ions amplifies the cytotoxicity of the probe, lowering its IC_{50} after 24 h from 6.03 μM to 1.91 μM, while that for the ligand ionophore **S2** decreased from >100 μM to 19.95 μM, indicating the important role of the metal center in conferring cytotoxicity. The stronger ability of complex **1** to deliver Cu^+ into mitochondria compared to **S2** (about 3-fold) was further verified using ICP-MS. In our system, the addition of serum enhanced the delivery of Cu^+ ions by complex **1** or provided additional Cu^+ ions, further lowering the IC_{50} to as low as 0.26 μM. The high cytotoxicity of the Cu^+-loaded probe **1** allows the use of Cu^+ ions at very low concentrations, decreasing the nonspecific toxicity caused by free Cu^+ ions. The key role of Cu^+ ions in mediating the cytotoxicity of complex **1** was confirmed when the Cu^+ chelator BCDS was co-administered, which rescued the cytotoxicity caused by the Cu^+-loaded probe **1**-treated cells by up to 75.81%. Finally, complex **1** and the Cu^+-loaded probe **1** at low concentration (1 μM) boosted the cuproptosis biomarker DLAT, while **S2** + Cu^+ and Cu^+ had minimal effects at the same concentration. Similar to other cuproptosis molecules, complex **1** also induced ROS production and decreased GSH, thereby amplifying the chemotherapeutic function of the iridium(III) core.

METHODS

Photophysical measurements

Luminescence emission spectra were recorded on a Hitachi F-4700 luminescence spectrophotometer at ambient temperature. The luminescence spectra of complex **1** were measured with an excitation wavelength of 330 nm. The excitation slit and emission slit were both set at 5.0 nm, the photomultiplier tube voltage was set at 500 V, with a scan speed of 1200 nm/min. UV-visible (UV-vis) absorption spectra were recorded on a Hitachi U-3900 UV-vis spectrophotometer. The luminescence lifetime of the complex was measured by time-correlated single-photon counting following excitation at 330 nm with a NanoLED light source.

Benesi-Hildebrand analysis

According to the luminescence titration data, the measured luminescence $[1/(I - I_0)]$ at 634 nm exhibited an excellent linear relationship with the value of $1/[Cu^+]$, and the association constant was calculated according the Benesi-Hildebrand equation:

$$\frac{1}{(I - I_0)} = \frac{1}{(I - I_{FS})} + \frac{1}{K(I - I_{FS})[Cu^+]}$$

where K is the association constant, I_0 represents the luminescence intensity of complex **1** without Cu^+ at 634 nm, I is the luminescence intensity of complex **1** at 634 nm, and I_{FS} is the luminescence intensity at the saturation.

Confocal imaging

MDA-MB-231 and MCF-10A cells were placed in glass-bottomed dishes (SPL Life Science, Kyong-Gi, South Korea). Following 24 h of incubation, the cells were treated with complex at the specified time intervals and concentrations. Subsequently, the cells were washed with PBS three times. Luminescence imaging of the complex within the cells was performed using a Leica TCS SP8 confocal laser-scanning microscope system with excitation at 405 nm.

Please see the supplemental methods for other details regarding the synthesis and characterization of the compounds, cell experiments, and *in vivo* biocompatibility assessment.

RESOURCE AVAILABILITY

Lead contact

Requests for further information and resources should be directed to and will be fulfilled by the lead contact, Chung-Hang Leung (duncanleung@um.edu.mo).

Materials availability

All unique or stable reagents generated in this study are available from the lead contact with a completed materials transfer agreement.

Data and code availability

The authors declare that the data supporting the findings of this study are available within the main text and the supplemental information. This paper does not report original code. All other data are available from the lead contact upon reasonable request.

ACKNOWLEDGMENTS

This work is supported by the National Natural Science Foundation of China (22101230); the Fundamental Research Funds for the Central Universities (D5000230060); the Key Research and Development Program of Shaanxi (2024SF-YBXM-418); the National Key Research and Development Program of China (2023YFE0205200); the Guangdong Basic and Applied Basic Research Foundation (2025A1515010971, 2023A1515011871); the Hainan Province Science and Technology Special Fund (ZDYF2021SHFZ250); the Innovation Capability Support Program of Shaanxi (2023-CX-TD-72); the Science and Technology Development Fund, Macau SAR, China (file no. 005/2023/SKL, 0020/2022/A1, 0045/2023/AMJ, and 0032/2023/RIB2); the University of Macau; the University of Macau Development Foundation, Macau SAR, China (file no. MYRG-GRG2023-00194-ICMS-UMDF and MYRG-GRG2024-00202-ICMS-UMDF); the State Key Laboratory of Quality Research in Chinese Medicine; and the University of Macau, Macau SAR, China (file no. SKL-QRCM-IRG2023-025).

AUTHOR CONTRIBUTIONS

J.D. and L. Wang, investigation, methodology, formal analysis, and writing – original draft; L. Wu, visualization and writing – review & editing; J.-B.L., resources, supervision, and funding acquisition; C.-H.L. and W.W., conceptualization, supervision, funding acquisition, and writing – review & editing.

DECLARATION OF INTERESTS

The authors declare no competing interests.

SUPPLEMENTAL INFORMATION

Supplemental information can be found online at https://doi.org/10.1016/j.xcrp.2025.102592.

CellPress
OPEN ACCESS

Received: November 3, 2024
Revised: February 19, 2025
Accepted: April 14, 2025
Published: May 7, 2025

REFERENCES

1. Guo, B., Yang, F., Zhang, L., Zhao, Q., Wang, W., Yin, L., Chen, D., Wang, M., Han, S., Xiao, H., and Xing, N. (2023). Cuproptosis induced by ROS responsive nanoparticles with elesclomol and copper combined with αPD-L1 for enhanced cancer immunotherapy. Adv. Mater. *35*, 2212267.
2. Pham, V.N., and Chang, C.J. (2023). Metalloallostery and transition metal signaling: bioinorganic copper chemistry beyond active sites. Angew. Chem. Int. Ed. *62*, e202213644.
3. Wang, W., Mo, W., Hang, Z., Huang, Y., Yi, H., Sun, Z., and Lei, A. (2023). Cuproptosis: Harnessing transition metal for cancer therapy. ACS Nano *17*, 19581–19599.
4. Tsvetkov, P., Coy, S., Petrova, B., Dreishpoon, M., Verma, A., Abdusamad, M., Rossen, J., Joesch-Cohen, L., Humeidi, R., Spangler, R.D., et al. (2022). Copper induces cell death by targeting lipoylated TCA cycle proteins. Science *375*, 1254–1261.
5. Kahlson, M.A., and Dixon, S.J. (2022). Copper-induced cell death. Science *375*, 1231–1232.
6. Zhou, J., Yu, Q., Song, J., Li, S., Li, X.L., Kang, B.K., Chen, H.Y., and Xu, J. J. (2023). Photothermally triggered copper payload release for cuproptosis-promoted cancer synergistic therapy. Angew. Chem. Int. Ed. *62*, e202213922.
7. Wang, W., Cui, Y., Wei, X., Zang, Y., Chen, X., Cheng, L., and Wang, X. (2024). $CuCo_2O_4$ nanoflowers with multiple enzyme activities for treating bacterium-infected wounds via cuproptosis-like death. ACS Nano *18*, 15845–15863.
8. Zhang, Y., Zhang, N., Xing, J., Sun, Y., Jin, X., Shen, C., Cheng, L., Wang, Y., and Wang, X. (2024). In situ hydrogel based on Cu–Fe_3O_4 nanoclusters exploits oxidative stress and the ferroptosis/cuproptosis pathway for chemodynamic therapy. Biomaterials *311*, 122675.
9. Hu, Z., Shan, J., Jin, X., Sun, W., Cheng, L., Chen, X.L., and Wang, X. (2024). Nanoarchitectonics of in situ antibiotic-releasing acicular nanozymes for targeting and Inducing cuproptosis-like death to eliminate drug-resistant bacteria. ACS Nano *18*, 24327–24349.
10. Yin, T., Yang, T., Chen, L., Tian, R., Cheng, C., Weng, L., Zhang, Y., and Chen, X. (2023). Intelligent gold nanoparticles for malignant tumor treatment via spontaneous copper manipulation and on-demand photothermal therapy based on copper induced click chemistry. Acta Biomater. *166*, 485–495.
11. Zhao, F., Yu, H., Liang, L., Wang, C., Shi, D., Zhang, X., Ying, Y., Cai, W., Li, W., Li, J., et al. (2023). Redox homeostasis disruptors based on metal-phenolic network nanoparticles for chemo/chemodynamic synergistic tumor therapy through activating apoptosis and cuproptosis. Adv. Healthc. Mater. *12*, 2301346.
12. Ge, E.J., Bush, A.I., Casini, A., Cobine, P.A., Cross, J.R., DeNicola, G.M., Dou, Q.P., Franz, K.J., Gohil, V.M., Gupta, S., et al. (2022). Connecting copper and cancer: from transition metal signalling to metalloplasia. Nat. Rev. Cancer *22*, 102–113.
13. Guo, Y., Fan, Y., Wang, Z., Li, G., Zhan, M., Gong, J., Majoral, J.P., Shi, X., and Shen, M. (2022). Chemotherapy mediated by biomimetic polymeric nanoparticles potentiates enhanced tumor immunotherapy via amplification of endoplasmic reticulum stress and mitochondrial dysfunction. Adv. Mater. *34*, 2206861.
14. Wang, W., Gao, P., Gui, H., Wei, X., Zhang, H., and Wang, X. (2025). Copper-based nanomaterials for the treatment of bacteria-infected wounds: material classification, strategies and mechanisms. Coord. Chem. Rev. *522*, 216205.
15. Huang, Z., Luo, Y., Zhang, T., Ding, Y., Chen, M., Chen, J., Liu, Q., Huang, Y., and Zhao, C. (2022). A stimuli-responsive small-molecule metal-carrying prochelator: A novel prodrug design strategy for metal complexes. Angew. Chem. Int. Ed. *61*, e202203500.
16. Vo, N.H., Xia, Z., Hanko, J., Yun, T., Bloom, S., Shen, J., Koya, K., Sun, L., and Chen, S. (2014). Synthesis, crystallographic characterization and electrochemical property of a copper(II) complex of the anticancer agent elesclomol. J. Inorg. Biochem. *130*, 69–73.
17. Wang, W., Wu, K.J., Vellaisamy, K., Leung, C.H., and Ma, D.L. (2020). Peptide-conjugated long-lived theranostic imaging for targeting GRPr in cancer and immune cells. Angew. Chem. Int. Ed. *59*, 17897–17902.
18. Ning, S., Lyu, M., Zhu, D., Lam, J.W.Y., Huang, Q., Zhang, T., and Tang, B. Z. (2023). Type-I AIE photosensitizer loaded biomimetic system boosting cuproptosis to inhibit breast cancer metastasis and rechallenge. ACS Nano *17*, 10206–10217.
19. Le Roy, M.M., Héry, S., Saffon-Merceron, N., Platas-Iglesias, C., Troadec, T., and Tripier, R. (2023). A Phosphine Oxide-Functionalized Cyclam as a Specific Copper (II) Chelator. Inorg. Chem. *62*, 8112–8122.
20. Xiang, J., Xiang, C., Zhou, L., Sun, M., Feng, L., Liu, C., Cai, L., and Gong, P. (2022). Rational design, synthesis of fluorescence probes for quantitative detection of amyloid-β in Alzheimer's disease based on rhodamine-metal complex. Anal. Chem. *94*, 11791–11797.
21. Phillips, K.A., Stonelake, T.M., Chen, K., Hou, Y., Zhao, J., Coles, S.J., Horton, P.N., Keane, S.J., Stokes, E.C., Fallis, I.A., et al. (2018). Ligand-tuneable, red-emitting iridium(III) complexes for efficient triplet–triplet annihilation upconversion performance. Chem. Eur J. *24*, 8577–8588.
22. Stonelake, T.M., Phillips, K.A., Otaif, H.Y., Edwardson, Z.C., Horton, P.N., Coles, S.J., Beames, J.M., and Pope, S.J.A. (2020). Spectroscopic and theoretical investigation of color tuning in deep-red luminescent iridium (III) complexes. Inorg. Chem. *59*, 2266–2277.
23. Zhang, W., Li, B., Ma, H., Zhang, L., Guan, Y., Zhang, Y., Zhang, X., Jing, P., and Yue, S. (2016). Combining ruthenium(II) complexes with metal–organic frameworks to realize effective two-photon absorption for singlet oxygen generation. ACS Appl. Mater. Interfaces *8*, 21465–21471.
24. Shanbhag, V.C., Gudekar, N., Jasmer, K., Papageorgiou, C., Singh, K., and Petris, M.J. (2021). Copper metabolism as a unique vulnerability in cancer. Biochim. Biophys. Acta. Mol. Cell Res. *1868*, 118893.
25. Bagheri, N., Mazzaracchio, V., Cinti, S., Colozza, N., Di Natale, C., Netti, P.A., Saraji, M., Roggero, S., Moscone, D., and Arduini, F. (2021). Electroanalytical sensor based on gold-nanoparticle-decorated paper for sensitive detection of copper ions in sweat and serum. Anal. Chem. *93*, 5225–5233.
26. Twomey, P.J., Viljoen, A., House, I.M., Reynolds, T.M., and Wierzbicki, A. S. (2005). Relationship between serum copper, ceruloplasmin, and non–ceruloplasmin-bound copper in routine clinical practice. Clin. Chem. *51*, 1558–1559.
27. Zuo, Y.-N., Liu, S., Zhao, X.-E., Zhu, S., and Xu, G. (2023). Tb-metal organic frameworks-referenced bathocuproine disulfonate enable fluorescence distinguishing Cu^+ from Cu^{2+}. Sensor. Actuator. B Chem. *394*, 134487.
28. Xu, Y., Liu, S.Y., Zeng, L., Ma, H., Zhang, Y., Yang, H., Liu, Y., Fang, S., Zhao, J., Xu, Y., et al. (2022). An enzyme-engineered nonporous copper (I) coordination polymer nanoplatform for cuproptosis-based synergistic cancer therapy. Adv. Mater. *34*, 2204733.
29. Wang, C., Yang, X., Dong, C., Chai, K., Ruan, J., and Shi, S. (2023). Cu-related agents for cancer therapies. Coord. Chem. Rev. *487*, 215156.
30. Qiao, L., Zhu, G., Jiang, T., Qian, Y., Sun, Q., Zhao, G., Gao, H., and Li, C. (2024). Self-destructive copper carriers induce pyroptosis and

cuproptosis for efficient tumor immunotherapy against dormant and recurrent tumors. Adv. Mater. *36*, 2308241.

31. Hao, D., Luo, W., Yan, Y., and Zhou, J. (2024). Focus on cuproptosis: Exploring new mechanisms and therapeutic application prospects of cuproptosis regulation. Biomed. Pharmacother. *178*, 117182.
32. Chan, L., Liu, Y., Chen, M., Su, Y., Guo, J., Zhu, L., Zhan, M., Chen, T., and Lu, L. (2023). Cuproptosis-driven enhancement of thermotherapy by sequentially response Cu_2-xSe via copper chemical transition. Adv. Funct. Mater. *33*, 2302054.
33. Kim, J., Choi, S., aek, J., Park, Y.I., Kim, J.C., Jeong, J., Jung, H., Kwon, T., Kim, B., and Lee, S. (2023). Design of topology-controlled polyethers toward robust cooperative hydrogen bonding. Adv. Funct. Mater. *33*, 2302086.
34. Su, T.A., Shihadih, D.S., Cao, W., Detomasi, T.C., Heffern, M.C., Jia, S., Stahl, A., and Chang, C.J. (2018). A modular ionophore platform for liver-directed copper supplementation in cells and animals. J. Am. Chem. Soc. *140*, 13764–13774.

Cell Reports Physical Science, Volume *6*

Supplemental information

A subcellular-specific iridium complex boosting cuproptosis for cancer theranostics

Jianxiong Du, Ling Wang, Lei Wu, Jin-Biao Liu, Chung-Hang Leung, and Wanhe Wang

Supplemental Methods and Figures

Part A: Chemicals and materials

Bis(pyridin-2-ylmethyl)amine, 4-HydroxyMethyl-4'-Methyl-2,2'-bipyridyl, 4-Nitrophenyl chloroformate purchased from Bide Pharmatech Co., Ltd. (Shanghai, China). 4-chloro-2-phenylquinoline purchased from Thermo Scientific, (Shanghai, China). Iridium chloride hydrate ($IrCl_3 \cdot xH_2O$) was purchased from J&K Chemical Ltd. (Beijing, China) and used as received. MDA-MB-231, MCF-10A cell lines were purchased from the American Type Culture Collection (Manassas, VA, USA). Fetal bovine serum (FBS) and Dulbecco's Modified Eagle's Medium (DMEM) were purchased from Gibco BRL (Gaithersburg, MD, USA). Cells were cultured in DMEM supplemented with 10% FBS in 5% CO_2 in a 37 ℃ incubator.

Part B: Synthesis experiments

Synthesis experiment

Mass spectrometry was performed at the Mass Spectroscopy Unit at the Institute of Medical Research, Northwestern Polytechnical University, Xi'an (China). Deuterated solvents for NMR purposes were obtained from Armar and used as received. ^{1}H and ^{13}C NMR were recorded on a Bruker Avance 500 spectrometer operating at 500 MHz (^{1}H) and 126 MHz (^{13}C), or a Bruker Avance 400 spectrometer operating at 400 MHz (^{1}H) and 100 MHz (^{13}C). ^{1}H and ^{13}C chemical shifts were referenced internally to solvent shift (^{13}C, 77.16; DMSO-d_6: ^{1}H, 2.50, ^{13}C, 39.52). Chemical shifts are quoted in ppm, the downfield direction being defined as positive. Uncertainties in chemical shifts are typically ±0.01 ppm for ^{1}H and ±0.05 for ^{13}C. Coupling constants are typically ±0.1 Hz for ^{1}H-^{1}H and ±0.5 Hz for ^{1}H-^{13}C couplings. The following abbreviations are used for convenience in reporting the multiplicity of NMR resonances: s, singlet; d, doublet; t, triplet; q, quartet; m, multiplet; br, broad. All NMR data were acquired and processed using standard Bruker software (Topspin) or MestreNova (Mestrelab).

Synthesis of compound S1

(3'-methyl-[1,1'-biphenyl]-3-yl)methanol (3 mmol) and p-nitrophenyl chloroformyl ester (6mmol) were mixed in DCM (30ml), at the same time adding pyridine (10mmol), stirring overnight at room temperature, directly purified by silica gel column chromatography to obtain the required product. Yield: 60%。 ^{1}H NMR (400 MHz, DMSO) δ 8.71 (d, J = 4.9 Hz, 1H), 8.55 (d, J = 4.9 Hz, 1H), 8.45 (s, 1H), 8.34 (d, J = 9.1 Hz, 2H), 8.26 (s, 1H), 7.63 (d, J = 9.0 Hz, 2H), 7.51 (d, J = 4.4 Hz, 1H), 7.31 (d, J = 4.6 Hz, 1H), 5.47 (s, 2H), 2.42 (s, 3H). ^{13}C

NMR (101 MHz, DMSO) δ 156.12, 155.68, 155.08, 152.33, 150.01, 149.55, 148.58, 145.71, 145.42, 125.93, 125.68, 123.11, 122.67, 121.77, 119.04), 69.00, 21.18. ESI-MS: Calcd. for $C_{19}H_{15}O_5N_3$ [M + H] 366.13. Found: 366.10.

Synthesis of compound S2

Compound **S1** (1 mmol), bis(Pyridin-2-ylamine)amine (1.5mmol) and DIPEA (5 mmol)were dissolved in DCM, stirred overnight at 60 ^{o}C, and purified directly by silica gel column chromatography to obtain the required product. Yield: 73%. ^{1}H NMR (400 MHz, DMSO) δ 8.58 (d, *J* = 4.8 Hz, 1H), 8.53 (dd, *J* = 10.1, 5.0 Hz, 3H), 8.28 – 8.20 (m, 2H), 7.73 (t, *J* = 7.6 Hz, 2H), 7.33 (d, *J* = 7.8 Hz, 2H), 7.25 (dd, *J* = 15.9, 4.8 Hz, 4H), 5.25 (s, 2H), 4.67 (t, *J* = 13.3 Hz, 4H), 2.41 (s, 3H). ^{13}C NMR (101 MHz, DMSO) δ 157.64, 156.19, 155.88, 155.30, 149.65, 149.52, 148.43, 147.73, 137.32, 125.53, 122.87, 121.91, 121.81, 121.75, 118.47, 116.27, 65.49, 53.28, 21.19.. ESI-MS: Calcd. for $C_{23}H_{29}O_3N_5$ [M + H] 426.18. Found: 426.18.

Synthetic procedure of complex 1

$IrCl_3 \cdot xH_2O$ was heated to 135 °C with 2.1 equivalents of the cyclometallated ligand 4-chloro-2-phenylquinoline (Clpq) in the mixture of methoxyethanol:H_2O (v/v, 3:1) under a nitrogen atmosphere overnight. The reaction was cooled to room temperature, and the product was filtered and washed with three portions of deionized water and then three portions of ether to yield the cyclometalated dichloro-bridged dimer ($Ir_2[Clpq]_4Cl_2$) without further purification. The complex were then synthesized using the prepared $Ir_2[Clpq]_4Cl_2$ and the ligand. A suspension of $Ir_2[Clpq]_4Cl_2$ (0.08 mmol) and compound **S2** (0.16 mmol) in a mixture of DCM : MeOH (1:1, 6 mL) was stirred under rt overnight. The reaction mixture was added with excess solid ammonium hexafluorophosphate (NH_4PF_6), and then stirred for another 0.5 h. The reaction mixture was purified by column chromatography to afford final complex **1**.

Complex 1: Yield: 72%. ^{1}H NMR (400 MHz, DMSO) δ 8.89 (d, *J* = 23.4 Hz, 2H), 8.45 (d, *J* = 8.0 Hz, 2H), 8.41 – 8.28 (m, 4H), 8.21 (d, *J* = 9.7 Hz, 5H), 8.10 (t, *J* = 8.3 Hz, 2H), 7.93 (dd, *J* = 9.6, 5.7 Hz, 2H), 7.73 (s, 1H), 7.55 (td, *J* = 18.0, 8.3 Hz, 5H), 7.43 (d, *J* = 5.9 Hz, 1H), 7.32 (t, *J* = 9.0 Hz, 3H), 7.26 – 7.16 (m, 5H), 7.05 (d, *J* = 7.2 Hz, 1H), 6.90 – 6.81 (m, 2H), 6.46 (t, *J* = 7.6 Hz, 2H), 5.21 (s, 2H), 4.67 (d, *J* = 30.2 Hz, 4H), 2.39 (s, 3H). ^{13}C NMR (101 MHz, DMSO) δ 170.34, 157.71, 157.32, 155.71, 155.20, 154.57, 152.37, 151.62, 150.95, 149.18, 147.82, 146.05, 145.45, 137.46, 134.38, 131.62, 128.80,128.60, 126.18, 125.23, 123.41, 123.09, 122.21, 121.98, 119.08, 54.04, 42.31, 21.23, 18.52, 17.16, 12.97.ESI-MS: Calcd. for $IrC_{55}H_{41}Cl_2O_2N_7$ [M + H] 1094.2328. Found: 1094.2369.

Purity experiment

The purity of complex **1** was examined by Waters E2695 high-performance liquid chromatography (HPLC) system using an Agilent Extend-C18 column (4.6 mm × 250 mm, 5 μm). The sample volume injected was 5 μL with a flow rate of 1.0 mL/min. Mobile phase A is Milli-Q H_2O (with 0.1% v/v trifluoroacetic acid (TFA)) and mobile phase B is Methanol (MeOH), respectively. The mobile phase gradient was initially set for 5% MeOH, 5–95% MeOH from 0 min to 30 min, and ended up as a 95% MeOH over the 30 min run time. UV absorbance was monitored at 254 nm.

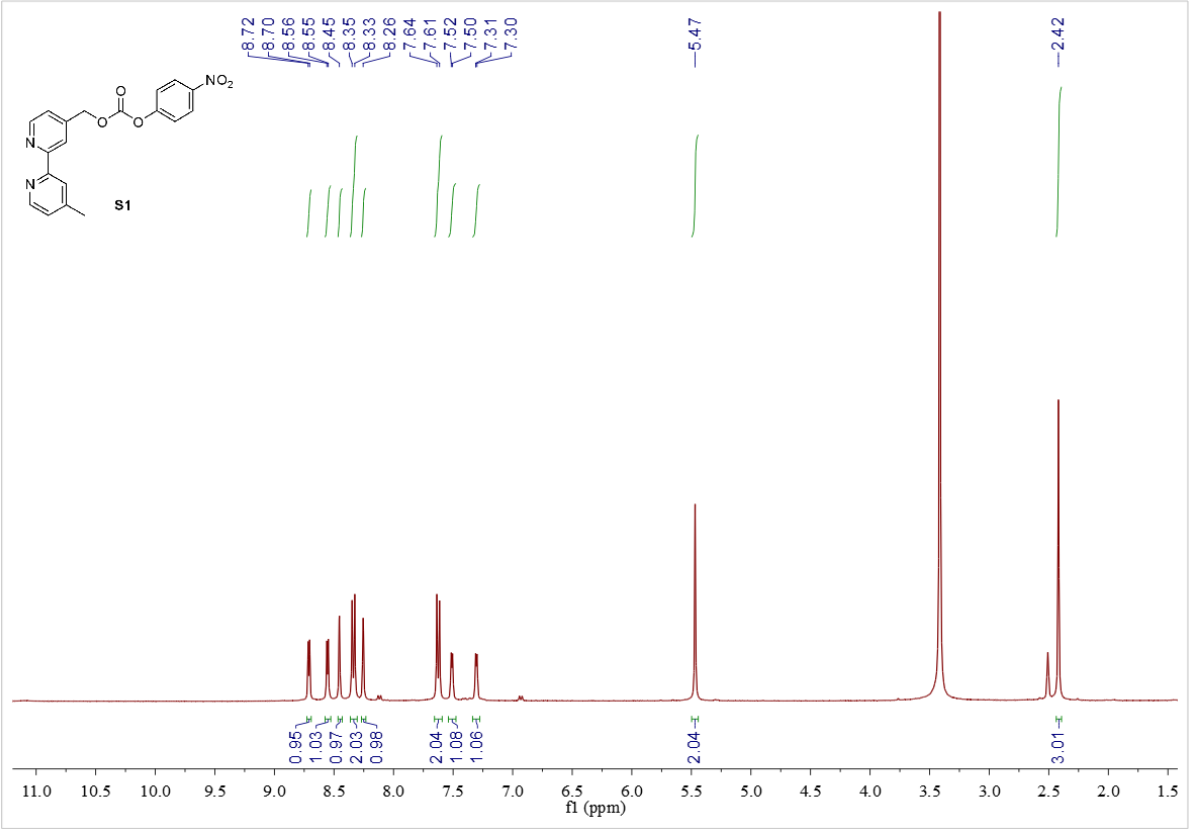

Figure S1. ^{1}H NMR spectrum of **S1** in DMSO-*d*.

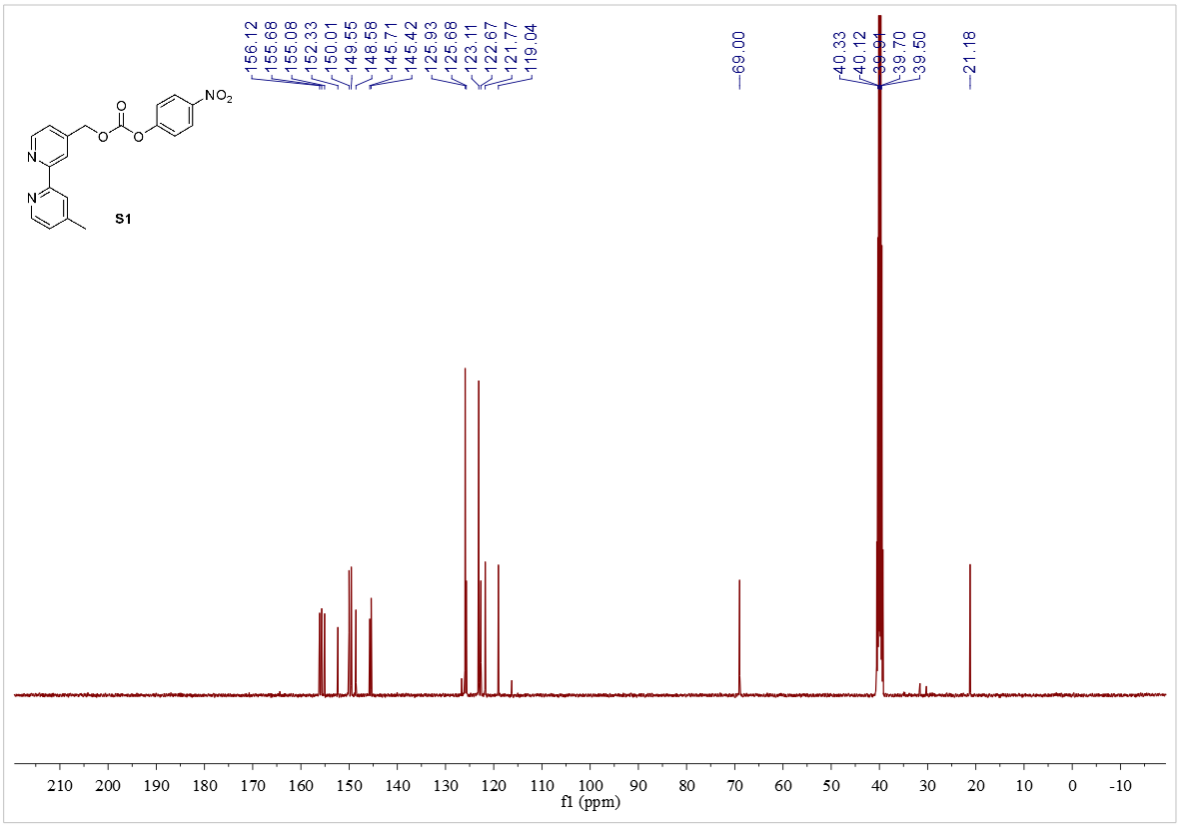

Figure S2. ^{13}C NMR spectrum of **S1** in DMSO-*d*.

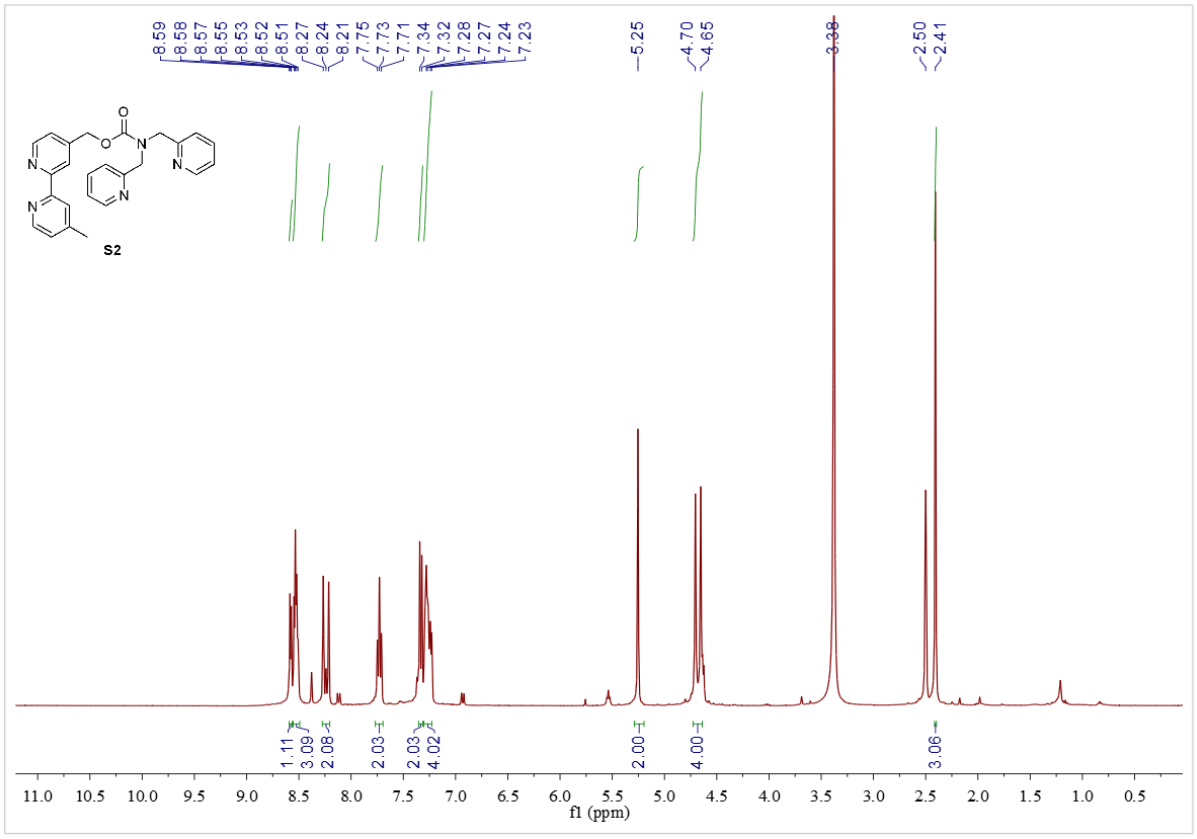

Figure S3. ^{1}H NMR spectrum of **S2** in DMSO-d.

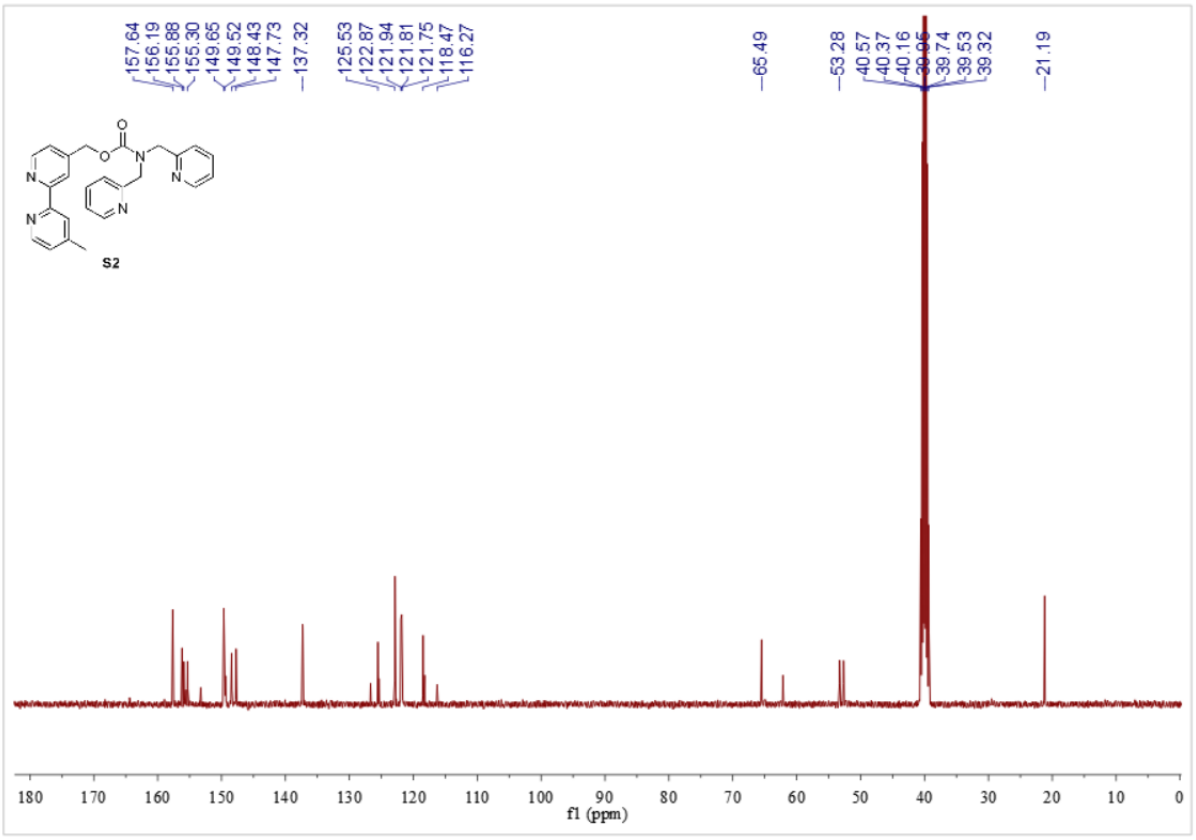

Figure S4. ^{13}C NMR spectrum of **S2** in DMSO-*d*.

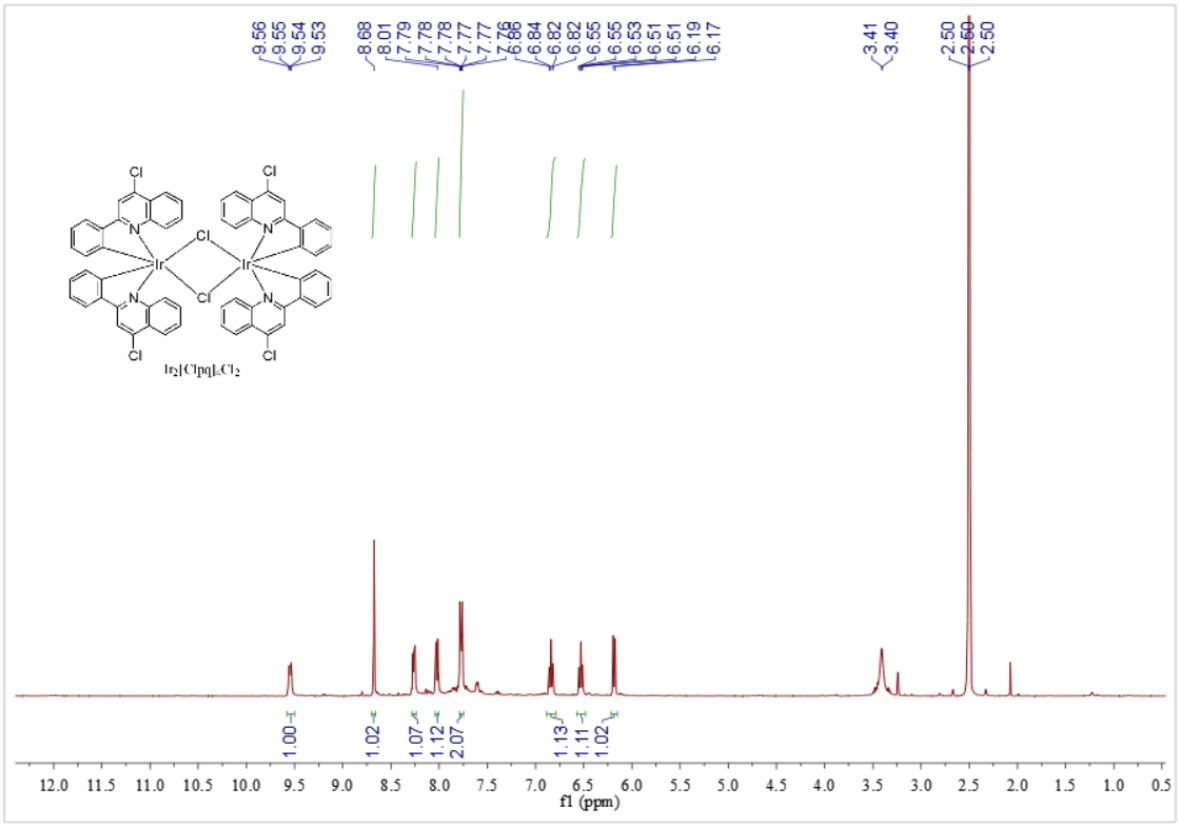

Figure S5. ^{1}H NMR spectrum of $Ir_2[Clpq]_4Cl_2$ in DMSO-*d*.

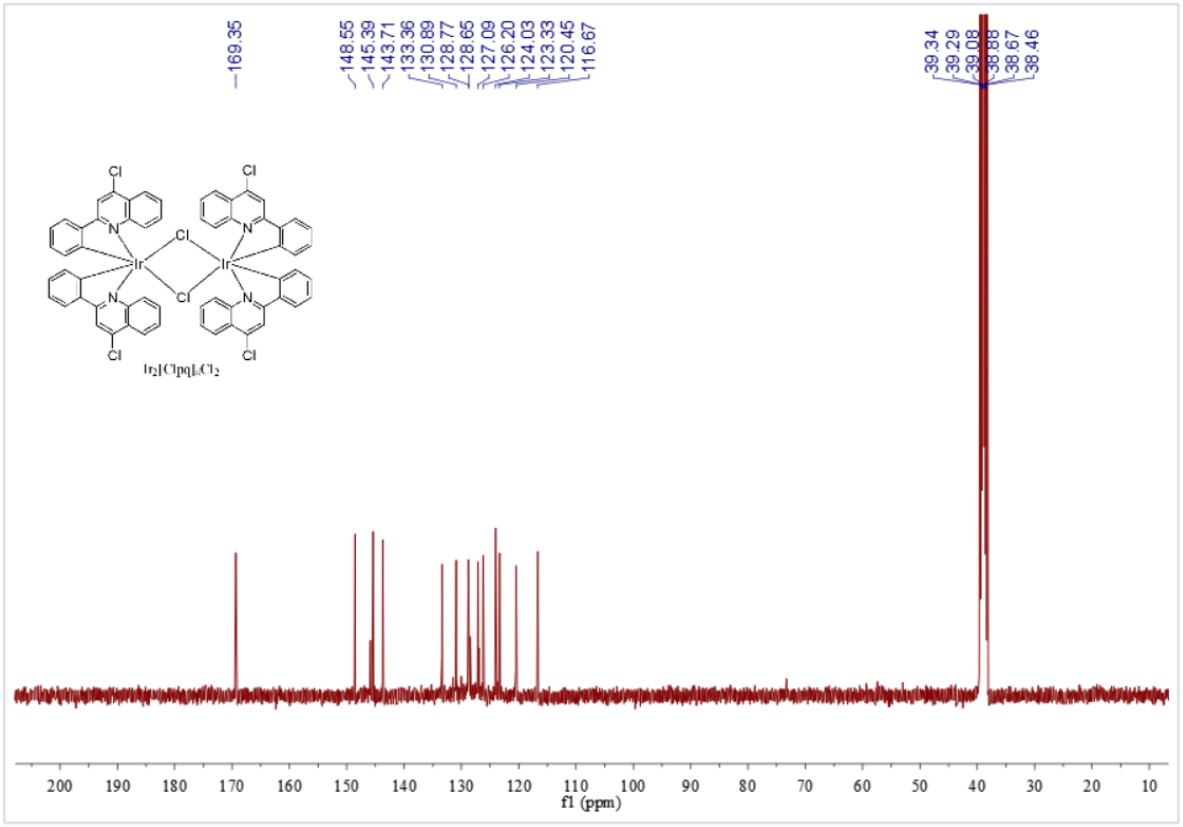

Figure S6. ^{1}C NMR spectrum of $Ir_2[Clpq]_4Cl_2$ in DMSO-*d*.

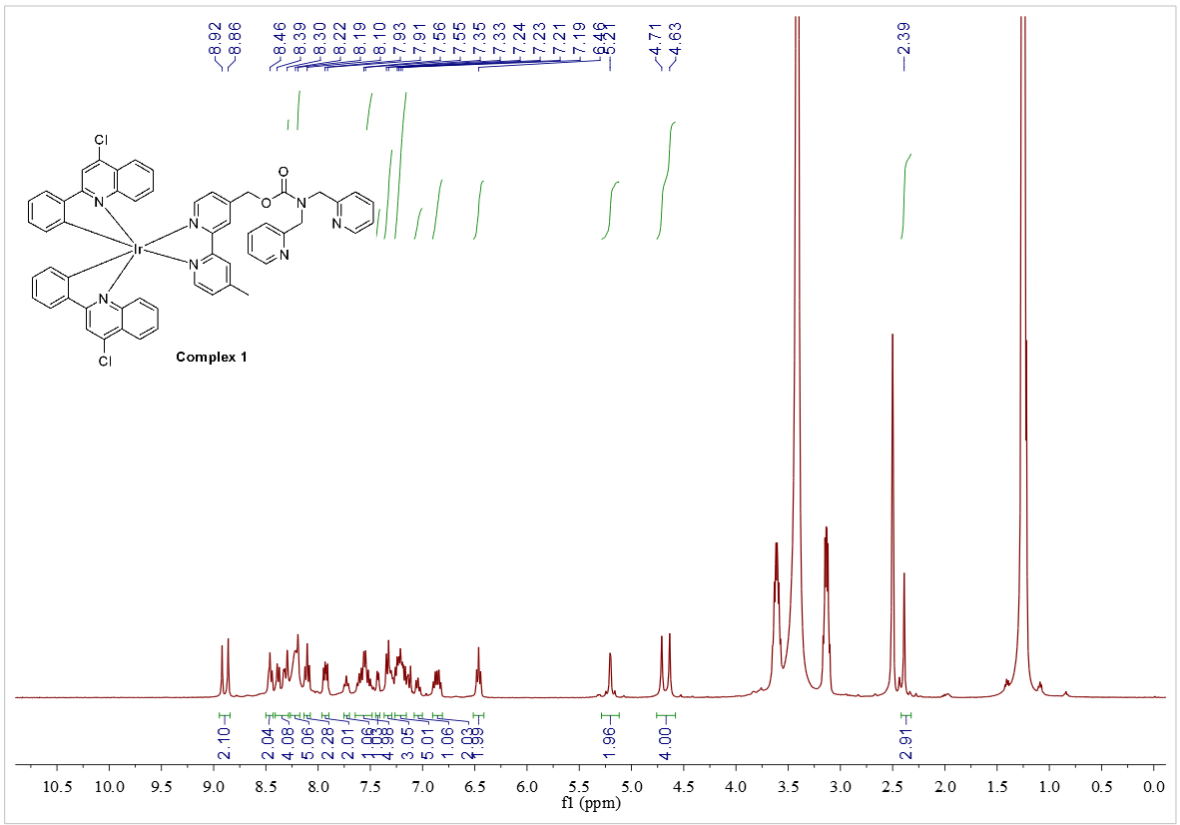

Figure S7. ^{1}H NMR spectrum of complex **1** in DMSO-*d*.

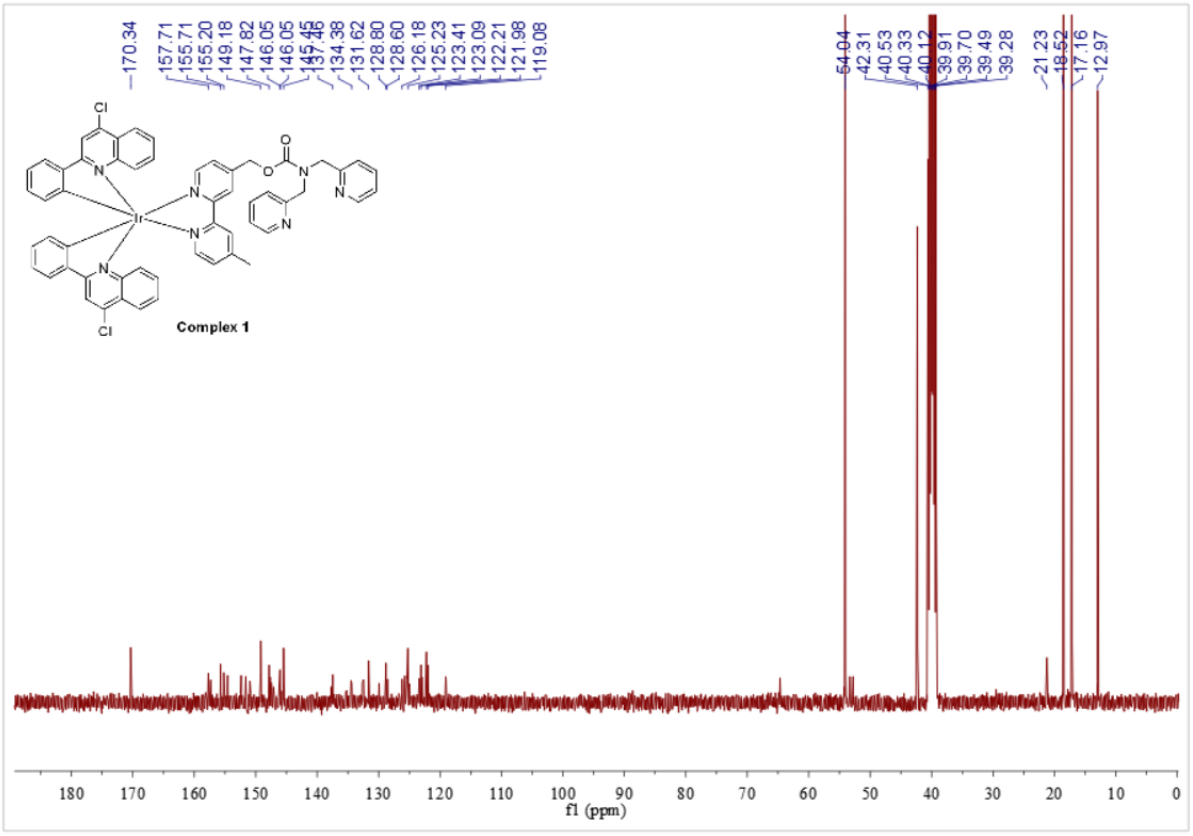

Figure S8. ^{1}H NMR spectrum of complex **1** in DMSO-*d*.

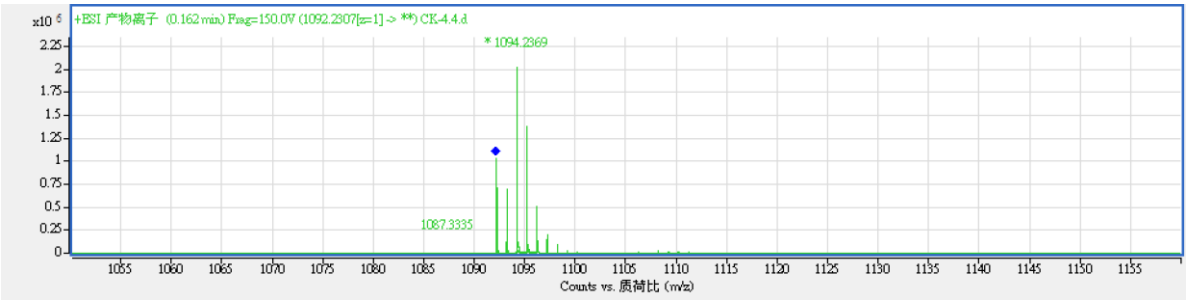

Figure S9. HRMS spectrum of complex **1**.

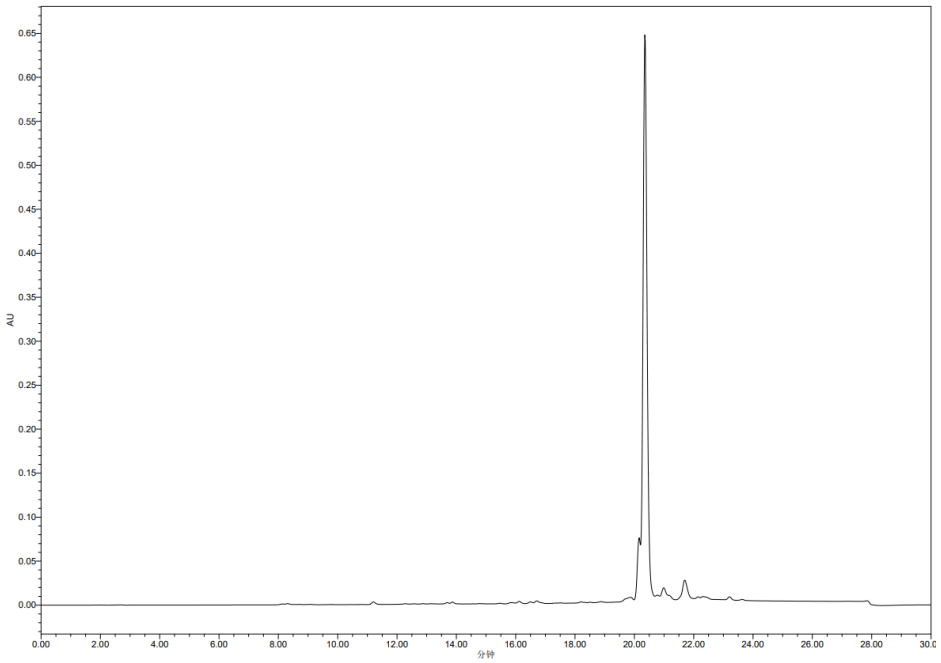

Figure S10. HPLC analysis of complex **1**. The absorbance was detected at 254 nm.

Part C: Biological experiments

MTT assay

MDA-MB-231 were seeded at a density of 8,000 cells per well in 96-well plates. After 24 h incubation, DMSO-dissolved complex **1**, the Cu^{+}-loaded probe **1**, **S2** or the Cu^{+}-loaded compound **S2** were added to cells at the indicated concentrations for 24 h, complex **1** and compound **S2** were pre-mixed with Cu^{+} in a concentration ratio of 1:1. Then, 25 μL of 5 mg/mL 3-(4,5-dimethylthiazol-2-yl)-2,5-diphenyltetrazoliumbromide (MTT) reagent was added to each well. After 4 h incubation in the dark, 100 μL of DMSO was added to each well, and the intensity of absorbance was determined by a SpectraMax M5 microplate reader at a wavelength of 570 nm.

Cell culture

MDA-MB-231 and MCF-10A cell lines were purchased from the American Type Culture Collection (Manassas, VA, USA). The cell lines of MCF-10A and MDA-MB-231 were cultured with Dulbecco's Modified Eagle's medium (DMEM, Gibco). Both media contain 10% fetal bovine serum (FBS, Gibco) and 1% penicillin/streptomycin (Gibco). Cells were cultured in a humidified air and 5% CO_2 atmosphere at 37 °C. For maintenance, the cells were cultured every 2 days.

Colocalization assay

MDA-MB-231 cells were seeded in a 35 mm confocal dish (SPL Life Sciences). Once the cell density reached approximately 80% confluency, the cells were washed thrice with PBS and then incubated with the Cu^{+}-loaded probe **1** at a concentration of 10 μM for 1 h. Following that, the cells were washed thrice with PBS again and incubated in DMEM medium (1% FBS) containing organelle trackers (Mito-tracker Red or Lyso-tracker Red) for 30 min. Finally, the cells were washed thrice with PBS. Cells were imaged using a Leica TCS SP8 confocal laser scanning microscope system.

ICP-MS assay

MDA-MB-231 cells were seeded in flasks at a density of 1×10^5/mL. Once the cell density reached approximately 80% confluency, the cells were treated with the Cu^{+}-loaded probe **1**, the Cu^{+}-loaded compound **S2** and Cu^{+} (10 μM) for 2 h. Cells were harvested, washed thrice with PBS, and cell fractions were obtained according to the instructions of the EpiQuik nuclear extraction kit and mitochondrial extraction kit (Beyotime Biotechnology). Finally, the samples were digested overnight with concentrated nitric acid, and the volume was made up to 5 mL with 2% nitric acid. The concentration of iridium was determined using ICP-MS. The remaining samples were used for Western blot analysis.

Immunofluorescence staining

For immunofluorescence experiments, MDA-MB-231 cells were plated on 35 mm cell dishes cultured 24 h prior to treatment with the Cu^{+}-loaded probe **1** (10 μM). The cells were fixed with 4% paraformaldehyde for 30 min, followed by permeabilized with 2% Triton X-100 for 15 min. Then, cells were blocked with 5% bovine serum albumin (BSA) for 30 min at room temperature followed by incubation with monoclonal anti-DLAT antibody (#12362S, CST) in 5% BSA for 2 h, then cells were incubated with the goat anti-rabbit IgG FITC tagged secondary antibody (A0562, Beyotime) in 5% BSA for 1 h at room temperature. Images were acquired on a Leica TCS SP8 confocal laser scanning microscope.

ROS measurement

Intracellular ROS levels were determined using a reactive oxygen species assay kit (Beyotime Biotechnology). MDA-MB-231 cells were treated with 1 μM complex **1**, the Cu^{+}-loaded probe **1**, and Cu^{+} for 12 h. Cells were harvested and stained with ROS reactive agent (DCFH-DA, 10 μM) in serum-free DMEM at 37 °C for 30 min. After washing with PBS twice, cells were imaged by confocal microscopy using excitation at 488 nm and emission at 525 nm.

Determination of intracellular GSH

MDA-MB-231 cells were treated with 1 μM complex **1**, the Cu^{+}-loaded probe **1**, Cu^{+} for 12 h. The level of intracellular GSH was determined using assay kits (Beyotime Biotechnology) in accordance with the manufacturer's instructions.

Western blotting

MDA-MB-231 cells were lysed and assayed for protein concentration using the BCA assay. Samples were resolved by SDS-polyacrylamide gel electrophoresis and transferred onto PVDF membranes (Millipore). Subsequently, membranes were treated with 5% non-fat milk in Tris-buffered saline containing 0.1% Triton X-100 (TBST) for 1 h. The membranes were probed with specific primary antibodies against DLAT, LIAS, Lamin B1, VDAC1, and GAPDH at 4 °C overnight and then with secondary antibodies at room temperature for 1 h. Proteins were stained with ECL Western Blotting Detection Reagent (GE Healthcare) and visualized using the ChemiDocTM MP Imaging System.

Animal experiment

Kunming mice (26 ± 2 g body weight) were purchased from Charles river Co., Ltd (Beijing, China). Mice were housed in groups of five per cage with ad libitum access to food and water. Rooms were temperature controlled (20 ± 1) °C, with a 12:12 dark:light cycles. After one week of adaptive feeding, the mice were divided into four groups (n = 5), and three groups were injected with three different doses of the Cu^{+}-loaded probe **1** (2.5, 5, 10 mg kg^{-1}) by intraperitoneal injection for seven consecutive times, respectively. PBS was used as a control group, and the weight of the mice was measured at a specified time point every day. The mice were euthanized after 2 weeks (the mice were anesthetized with 2% isoflurane). Major organs including the heart, liver, spleen, lung, and kidney were isolated. Moreover, histopathological sections of collected organs of each groups were prepared and stained with hematoxylin and eosin, followed by imaging with optical microscopy. The animals used in this study complied with the guidelines established by the American Society of Physiology. All animal protocols were approved by Animal Care and Use commite of Northwestern Polytechncial University (Approval number: 202401161).

Statistical analysis

The statistical analysis was carried out with GraphPad Prism 7 (GraphPad Software, La Jolla, USA). All data are expressed as means ± S.D. (n = 3), *P* values were calculated using the two-sided t-test. $*p < 0.05$, $**p < 0.01$ vs. indicated group were considered statistically significant.

Table S1. Photophysical properties of the complex in PBS buffer.

Complex	λ_{emi} (λ_{exc}) / nm	Quantum yield[a] / %	Lifetime /μs	UV/Vis absorption λ_{abs} / nm (ε / dm^3 mol^{-1} cm^{-1})
1	634 (345)	1.41	878	295 (0.18×10^5) 352 (0.12×10^5) 460 ($0.38 \times 10^{4)}$

Note: [a] means the measurement was performed in air-aerated solution.

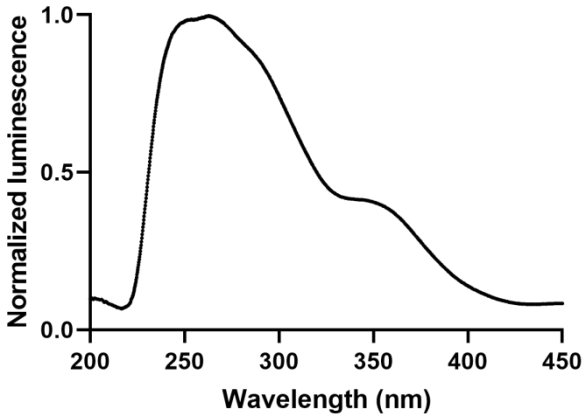

Figure S11. (a) Excitation spectra of 10 μM complex **1** in PBS λ_{emi} was set at 634 nm.

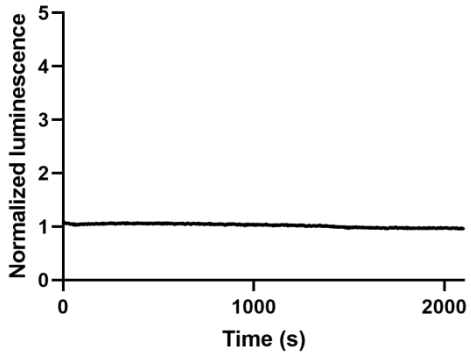

Figure S12. Luminescence intensity at 634 nm of complex **1** (10 μM) under UV irradiation at 365 nm for 2100 s in 10 mM PBS (pH = 7.4).

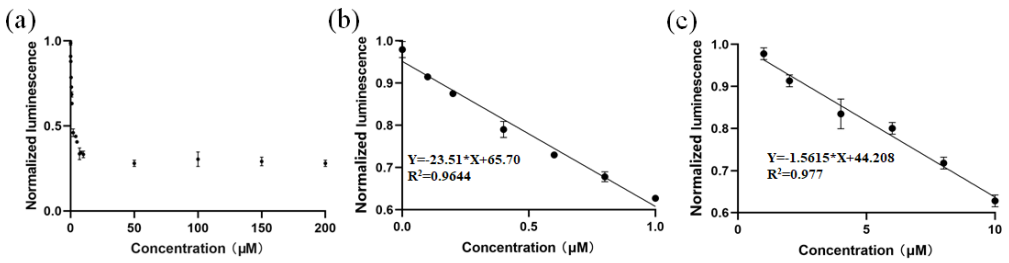

Figure S13. The linear relationship between luminescence intensity at 645 nm of complex **1** (10 μM) and Cu^{+} concentrations (0.1−1.0 and 1.0−10.0 μM).

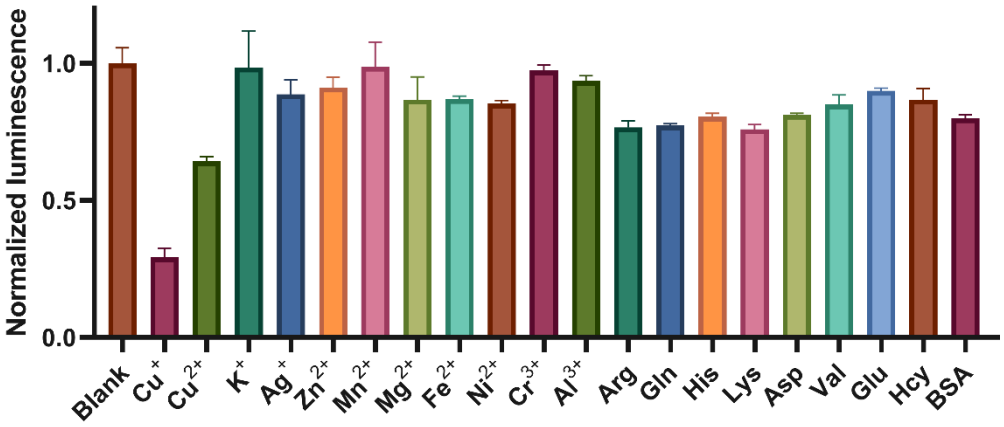

Figure S14. Luminescent response of complex **1** to various analytes. Complex **1** (10 μM) was incubated with 100 μM of other interferences under ambient temperature for 0.5 h in 10 mM PBS (pH = 7.4). Excitation was set at 345 nm and emission was set at 634 nm.

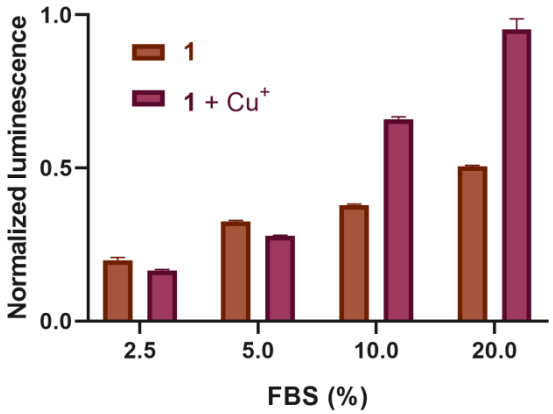

Figure S15. Complex **1** (10 μM) and the Cu^{+}-loaded probe **1** (10 μM) were incubated with different concentrations of FBS in 10 mM PBS (pH = 7.4) at room temperature for 0.5 h. Excitation was set at 345 nm and emission was set at 634 nm.

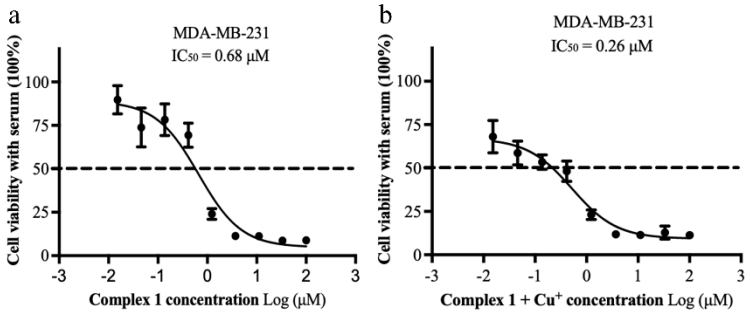

Figure S16. The cytotoxicity effect of complex **1**, the Cu^{+}-loaded probe **1** (0−100 μM) on MDA-MB-231 cells with serum culture as determined by an MTT assay. MDA-MB-231 cells were exposed to the indicated concentrations of (a) complex **1**, (b) the Cu^{+}-loaded probe **1** for 24 h, and cell viability was measured.

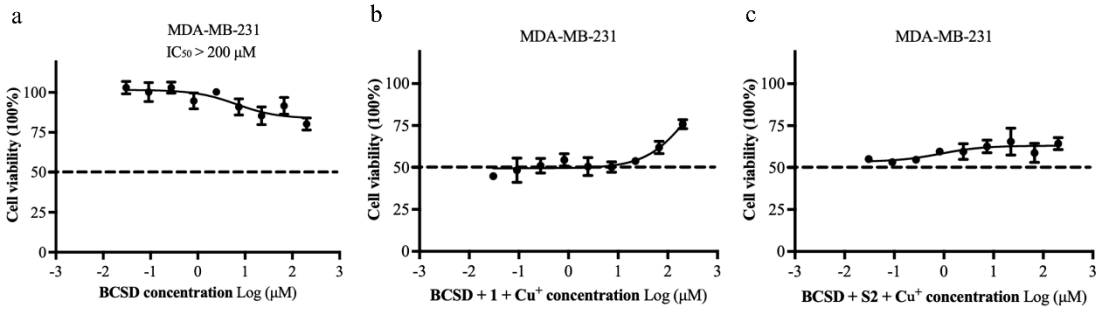

Figure S17. (a) The cell viabilities of MDA-MB-231 cells treated with different concentrations of **BCDS** (0−200 μM). (b) The cell viabilities of MDA-MB-231 cells treated with different concentrations of **BCDS** (0−200 μM), in the presence of the Cu^{+}-loaded probe **1** (1.91 μM); (c) The cell viabilities of MDA-MB-231 cells treated with different concentrations of **BCDS** (0−200 μM), in the presence of **S2** + Cu^{+} (20 μM);

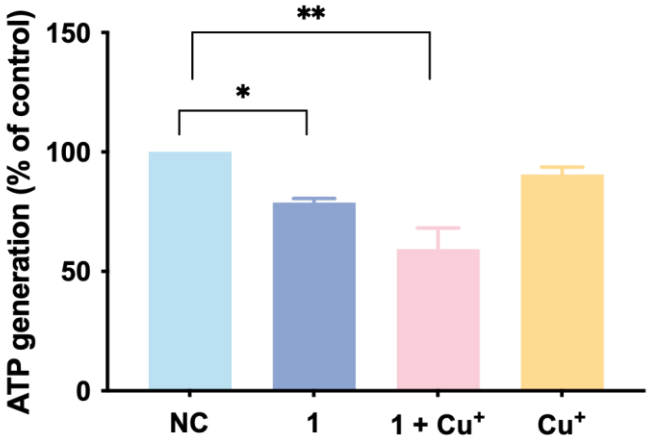

Figure S18. The mitochondrial ATP production capacity was significantly inhibited by complexes **1**, the Cu^{+}-loaded probe **1** in MDA-MB-231 cells, after treatment with complexes

1, the Cu^{+}-loaded probe **1** and Cu^{+} (1 μM) for 12 h. Data are presented as mean ± S.D. (n = 3). * $p < 0.05$, ** $p < 0.01$.

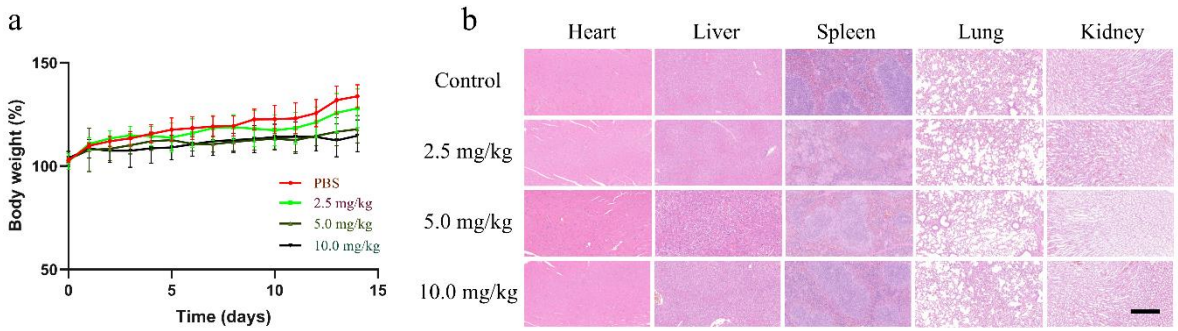

Figure S19. *In vivo* biocompatibility evaluation of complex **1.** (a) Change in body weight of mice injected with the Cu^{+}-loaded probe **1** with different doses (2.5, 5, 10 mg kg^{-1}) compare with those injected with PBS (mean ± SD, n = 5). (b) Histopathological image of major organs of the mice after 14 days treatment with the Cu^{+}-loaded probe **1** with different doses (2.5, 5, 10 mg kg^{-1}). mean ± S.D., n = 5. Scale bar: 50 μm.